

Graphical Abstract

Region-adaptable retrieval of coastal biogeochemical parameters from near-surface hyperspectral remote sensing reflectance using physics-aware meta-learning

Yiqing Guo^a, Nagur R. C. Cherukuru^b, Eric A. Lehmann^a, S. L. Kesav Unnithan^{b,c}, Tim J. Malthus^d, Gemma Kerrisk^e, Xiubin Qi^e, Faisal Islam^{d,f}, Tisham Dhar^g, Mark J. Doubell^h

Region-adaptable retrieval of coastal biogeochemical parameters from near-surface hyperspectral remote sensing reflectance using physics-aware meta-learning

Physical principles

Proposed two-stage approach
Physics-aware meta-learning
+
Region-specific adaptation

Regional distinctions



Highlights

Region-adaptable retrieval of coastal biogeochemical parameters from near-surface hyperspectral remote sensing reflectance using physics-aware meta-learning

Yiqing Guo^a, Nagur R. C. Cherukuru^b, Eric A. Lehmann^a, S. L. Kesav Unnithan^{b,c}, Tim J. Malthus^d, Gemma Kerrisk^e, Xiubin Qi^e, Faisal Islam^{d,f}, Tisham Dhar^g, Mark J. Doubell^h

- A physics-aware meta-learning method is proposed for region-adaptable hyperspectral retrieval of coastal biogeochemical (BGC) parameters.
- Experiments were conducted across five Australian coastal sites with clear regional distinctions in bio-optical and BGC characteristics.
- Results indicate that physics-aware pretraining and region-specific adaptation improved BGC retrieval accuracies.

Region-adaptable retrieval of coastal biogeochemical parameters from near-surface hyperspectral remote sensing reflectance using physics-aware meta-learning

Yiqing Guo^a, Nagur R. C. Cherukuru^b, Eric A. Lehmann^a, S. L. Kesav Unnithan^{b,c}, Tim J. Malthus^d, Gemma Kerrisk^d, Xiubin Qi^e, Faisal Islam^{d,f}, Tisham Dhar^g, Mark J. Doubell^h

^aCSIRO Data61, Acton, 2601, ACT, Australia

^bCSIRO Environment, Acton, 2601, ACT, Australia

^cCSIRO Space and Astronomy, Acton, 2601, ACT, Australia

^dCSIRO Environment, Dutton Park, 4102, QLD, Australia

^eCSIRO Space and Astronomy, Kensington, 6151, WA, Australia

^fQueensland Department of the Environment, Tourism, Science and Innovation, Brisbane, 4000, QLD, Australia

^gCSIRO Space and Astronomy, Adelaide, 5000, SA, Australia

^hSouth Australia Research and Development Institute, Aquatic Sciences, West Beach, 5024, SA, Australia

Abstract

Hyperspectral in situ sensing has shown promise in retrieving aquatic biogeochemical (BGC) parameters, such as total suspended solids, dissolved organic carbon, and total chlorophyll-a, for cost-effective monitoring of coastal water quality. However, generalising such retrieval algorithms across water bodies remains challenging, as the relationship between remote sensing reflectance (R_{rs}) and BGC parameters can vary considerably from one region to another due to regional distinctions in environmental conditions and biogeochemistry that lead to different BGC ranges and bio-optical properties. In this study, we propose a two-stage physics-aware meta-learning framework for retrieving coastal BGC parameters from near-surface R_{rs} observations. In the first stage, a bio-optical forward model is used to generate a large synthetic dataset based on an in situ bio-optical spectral library with broad representativeness of Australian coastal waters. This dataset is then used to pretrain a region-agnostic base model with meta-learning, allowing the model to learn fundamental physical relationships. In the second stage, the pretrained base model is fine-tuned for specific regions with local samples. To evaluate the proposed approach, we collected in situ hyperspectral R_{rs} and BGC measurements from five geographically distinct sites in Australian coastal waters. Our experimental results suggest the following: (1) the BGC parameters and their corresponding hyperspectral R_{rs} signatures exhibited clear regional distinctions among the experimental sites; (2) the synthetic dataset, generated under guidance of the bio-optical forward model and the bio-optical spectral library, was physically plausible and closely aligned with real-world samples in both parameter distributions and inter-parameter correlations; (3) benefiting from its physics-aware pretraining and region-adaptable fine-tuning, the proposed approach outperformed five benchmark models in BGC retrieval; and (4) time series of in situ measured and model-predicted BGC parameters showed good agreement in both magnitude and temporal dynamics, highlighting the potential of in situ hyperspectral sensing as a cost-effective solution for continuous time-series monitoring of coastal water quality. These results demonstrate that the proposed physics-aware

meta-learning framework provides a robust and adaptable approach for accurate BGC retrieval across diverse coastal environments using hyperspectral in situ sensing.

Keywords: coastal water quality, biogeochemical parameters, hyperspectral data, physics-aware learning, meta-learning, total suspended solids, dissolved organic carbon, total chlorophyll-a

1. Introduction

Water quality is an important indicator of aquatic ecosystem health, affecting biodiversity, productivity, and the provision of ecosystem services (Zhi et al., 2024; Lehmann et al., 2023; Unnithan et al., 2025). Degradation of water quality in aquatic systems undermines ecosystem functions and services, and potentially negatively impacts fisheries, aquaculture, and tourism (De Valck and Rolfe, 2018; Anderson et al., 2012; Medina et al., 2026). Timely, accurate, and continuous monitoring of water quality is therefore critical for effective management and mitigation of environmental impacts, particularly in Australian coastal waters where many regions are vulnerable to anthropogenic pressures and climate-driven change (Schaffelke et al., 2012; Unnithan et al., 2025; Guo et al., 2025a).

Key indicators of water quality include biogeochemical (BGC) parameters, such as total suspended solids (TSS), dissolved organic carbon (DOC), total chlorophyll-a (TChl-a), and their inherent optical properties (IOPs) (*e.g.*, O’Shea et al. (2023), Lou et al. (2025), and Luo et al. (2025)). TSS represents all particulate matter suspended in the water column (Baker and Lavelle, 1984) including phytoplankton and non-algal particles (NAP). Phytoplankton pigments, with TChl-a frequently used as the primary indicator of phytoplankton biomass, are widely used as a proxy for phytoplankton abundance and potential photosynthetic capacity (Huot et al., 2007). NAP is the fraction of TSS that excludes phytoplankton, consisting mainly of inorganic mineral particles and non-pigmented organic detritus (Babin et al., 2003). In addition to suspended particulates, dissolved components also play a critical role in the bio-optical properties of natural waters (Nelson and Siegel, 2013). Dissolved organic carbon (DOC) represents the carbon content of the diverse pool of dissolved organic matter (DOM) (Hansell and Carlson, 1998; Hansell et al., 2009), while its optically active fraction, known as chromophoric dissolved organic matter (CDOM), is widely used as a proxy for the source and compositional characteristics of DOM (Del Vecchio and Blough, 2004). The IOPs, including absorption and scattering coefficients, serve as the optical fingerprints of BGC parameters, characterising the intrinsic interactions between water constituents and light, and providing the foundation for bio-optical modelling (Lee et al., 2002). The mass-normalised IOPs, known as specific IOPs (SIOPs), describe how efficiently substances in water absorb or scatter light per unit concentration (Lee et al., 2002). Accurate local calibration of SIOPs is essential, as they may vary from one region to another due to differences in the composition and physiology of phytoplankton community, the size distributions of suspended particles, and the sources and processing of CDOM (Werdell et al., 2013; Cherukuru et al., 2020). Collectively,

these properties provide a basis for assessing water quality by optical means and for tracking changes in aquatic ecosystem conditions over time.

Traditional water quality monitoring relies on laboratory analysis of grab samples to derive BGC parameters (*e.g.*, Cherukuru et al. (2017)). While these methods are accurate and well-established, they are often labour-intensive, costly, and logistically constrained (Unnithan et al., 2025; Luo et al., 2025). Remote sensing has emerged as a cost-effective approach to retrieve key BGC parameters remotely (Zhi et al., 2024; Jiang et al., 2023; Zhang et al., 2025; Gui et al., 2026), and hyperspectral observations are particularly well-suited for capturing the spectral signatures required to assess water quality conditions (Abd-Elrahman et al., 2011; Lehmann et al., 2023; O’Shea et al., 2023). The optically active constituents, including phytoplankton pigments, NAP, and CDOM, jointly determine the optical properties of aquatic systems, with phytoplankton and NAP contributing to both absorption and scattering, and CDOM primarily affecting absorption (Babin et al., 2003). Hyperspectral sensors exploit these interactions by measuring water-leaving remote sensing reflectance (R_{rs}) across hundreds of contiguous spectral bands. The high spectral resolution enables the disentanglement of overlapping absorption features, isolation of constituent contributions, and simultaneous retrieval of multiple BGC parameters (O’Shea et al., 2023; Unnithan et al., 2025; Luo et al., 2025). Recent advances in data-driven algorithms, particularly those leveraging rigorous machine learning and deep learning frameworks, have shown promise for improving the accuracy and robustness of BGC parameter retrieval from hyperspectral R_{rs} measurements (*e.g.*, O’Shea et al. (2023), Luo et al. (2025), and Lou et al. (2025)).

Previous studies have identified that algorithms developed and validated within a particular region for retrieving BGC parameters may exhibit limited transferability to other regions with optically distinct waters (Mélin and Vantrepotte, 2015; Spyarakos et al., 2018). This lack of generalisation stems from the fact that the relationship between hyperspectral R_{rs} and BGC parameters is not universal, but rather depends on regional differences in environmental conditions and biogeochemistry that lead to distinct BGC ranges and SIOP characteristics (Werdell et al., 2013; Neil et al., 2019; O’Shea et al., 2023). Several seminal works have observed such regional distinctions in the relationship between BGC parameters and hyperspectral R_{rs} , and proposed strategies to address it. For example, Mao et al. (2012) reported that some regions in the East China Sea exhibit extremely high total suspended matter (TSM), exceeding the valid range of standard retrieval algorithms. To address this, the authors proposed a complex-proxy TSM model that blends four R_{rs} -based indices to transform the non-linear TSM– R_{rs} relationship into a quasi-linear one, enabling robust retrievals across the full concentration range. Ogashawara et al. (2016) observed that the Funil and Itumbiara reservoirs in Brazil are dominated by CDOM as the primary optically active constituent, whereas standard quasi-analytical algorithms (QAAs), originally designed for phytoplankton-dominated waters, failed to accurately retrieve the IOPs. To overcome this limitation, the QAA was re-parameterised by Ogashawara et al. (2016) to suit these CDOM-dominated

conditions. In a study to retrieve chlorophyll-a concentrations in 185 inland and coastal water bodies worldwide, Neil et al. (2019) demonstrated that improved retrieval accuracies could be achieved when algorithms are optimised for individual optical water types. These regional bio-optical distinctions contribute to the non-unique inverse problem (O’Shea et al., 2023), as the same (or nearly identical) spectral signatures of R_{rs} may correspond to different values of BGC parameters across water bodies. Therefore, robust and transferable algorithms for retrieving BGC parameters require explicit accommodation of such regional variations in bio-optical conditions.

In addition to handling regional bio-optical distinctions, data-driven water quality retrieval from hyperspectral R_{rs} measurements faces further challenges. The first challenge is that data-driven algorithms, especially those based on deep neural networks, require a sufficiently large amount of data samples for training, which are often hard to obtain as the collection of in situ samples is both labour-intensive and time-consuming. Several strategies have been implemented to handle this challenge, including: (1) self-supervised pretraining on unlabelled hyperspectral R_{rs} spectra is used to learn general representations, thereby reducing the number of labelled BGC- R_{rs} pairs required for subsequent model fine-tuning (Luo et al., 2025); and (2) aggregating samples from multiple sources into large, curated datasets, *e.g.* GLORIA (Lehmann et al., 2023), to facilitate the development of generalisable and adaptive models (O’Shea et al., 2023). Despite these efforts, the scarcity of in situ samples remains a major bottleneck, especially for developing region-specific models, as collecting enough samples for each region is costly and sometimes practically infeasible. The second challenge is that existing data-driven algorithms for hyperspectral retrieval of BGC parameters often rely on observational data only for model training without integrating knowledge of the underlying physical principles of underwater optics. This may limit the generalisability and interpretability of the developed models. Bringing physical principles into the learning process (*i.e.*, physics-aware learning) would help constrain solutions to physically plausible ranges, reduce the amount of labelled samples required during training, and regulate the model to lower the risk of overfitting to noisy samples in the dataset.

To alleviate these challenges, we propose a two-stage training framework in this study: (1) a physics-aware pretraining stage, and (2) a region-specific adaptation stage. In the pretraining stage, a physics-based bio-optical model is used to synthesise a BGC- R_{rs} dataset from a bio-optical library of in situ measured BGC parameters and IOPs/SIOPs with broad representativeness of Australian coastal waters. This synthetic dataset is applied to train a region-agnostic base model within a physics-aware meta-learning framework. In the adaptation stage, the pretrained base model is subsequently adapted to individual regions using in situ measured BGC- R_{rs} samples specific to each region. The base model can regulate regional adaptation by leveraging physical knowledge learned from pretraining, potentially reducing the amount of labelled samples required for regional fine-tuning. The proposed algorithm is designed to incorporate the following features that distinguish it from existing data-driven approaches to BGC retrieval from hyperspectral R_{rs} observations:

1. Integration of physical principles within a data-driven deep learning framework, enabling more robust modelling of the BGC– R_{rs} relationship and ensuring that the retrieved BGC parameters remain physically plausible; and
2. Adaptability to account for region-specific bio-optical distinctions in the BGC– R_{rs} relationship, thereby improving retrieval accuracies within each region.
3. Alleviated requirement of region-specific in situ samples for training, by leveraging a pretrained physics-aware model that can efficiently regulate the regional adaptation.

Supported by CSIRO’s AquaWatch Australia¹, we established four experimental sites in Australian waters, namely the Fitzroy Estuary and Keppel Bay sites in Queensland, the Boston Bay site in South Australia, and the Cockburn Sound site in Western Australia. Time-series measurements of in situ BGC parameters and hyperspectral R_{rs} were collected at these sites across multiple seasons from 2022 to 2025. In situ measurements were also sourced from a long-term monitoring site, namely the Lucinda Jetty Coastal Observatory in Queensland, from 2019 to 2023. These five sites cover several climate zones, including tropical, subtropical, and temperate, and represent a range of hydrodynamic regions, including riverine, estuarine, and coastal. As a result, the waters at these sites exhibit distinct bio-optical characteristics.

The proposed model for retrieving BGC parameters was evaluated using data collected from the aforementioned sites. Through quantitative analysis of the evaluation results, we aim to address primarily the following important questions:

1. Is there a clear regional distinction among the experimental sites in terms of BGC parameters and their hyperspectral R_{rs} signatures?
2. How does the proposed approach perform in hyperspectral retrieval of BGC parameters compared to benchmark algorithms?

The rest of this article is organised as follows. Section 2 describes the study sites, in situ hyperspectral R_{rs} and BGC measurements, and the bio-optical spectral library used in this study. Section 3 details the proposed physics-aware meta-learning framework, including the bio-optical forward model, synthetic data generation, model pretraining, and region-specific adaptation. Section 4 presents the experimental results and discusses the retrieval performance, regional variability, and time-series monitoring capabilities of the proposed approach. The key findings, limitations, and future directions are also discussed in Section 4. Finally, Section 5 concludes this article with a summary overview of this study. To facilitate readability, Table 1 lists the commonly used symbols and acronyms in this article.

¹<https://www.csiro.au/en/about/challenges-missions/AquaWatch>

Table 1: Symbols and acronyms used in this study. Only a subset is listed here, mainly those appearing in multiple sections.

Symbol/Acronym	Unit	Definition
<i>Biogeochemical (BGC) Parameters</i>		
TSS	mg/L	Total suspended solids concentration
TChl-a	$\mu\text{g/L}$	Total chlorophyll-a concentration
NAP	mg/L	Non-algal particles concentration
DOC	mg/L	Dissolved organic carbon concentration
<i>Inherent Optical Properties (IOPs)</i>		
a	m^{-1}	Total absorption coefficient
a_w	m^{-1}	Absorption coefficient of pure water
a_d	m^{-1}	Absorption coefficient of NAP
a_{ph}	m^{-1}	Absorption coefficient of phytoplankton
a_y	m^{-1}	Absorption coefficient of chromophoric dissolved organic matter (CDOM)
S_y	nm^{-1}	Spectral slope of CDOM absorption coefficient
b_b	m^{-1}	Total backscattering coefficient
b_{bw}	m^{-1}	Backscattering coefficient of pure water
b_{bp}	m^{-1}	Backscattering coefficient of particulate matter
S_{bbp}	–	Spectral slope of particulate backscattering coefficient
<i>Specific IOPs (SIOPs)</i>		
a_d^*	$\text{m}^2 \text{g}^{-1}$	Mass-specific absorption coefficient of NAP
a_{ph}^*	$\text{m}^2 \text{mg}^{-1}$	Mass-specific absorption coefficient of phytoplankton
a_y^*	$\text{m}^2 \text{g}^{-1}$	Mass-specific absorption coefficient of CDOM
b_{bp}^*	$\text{m}^2 \text{g}^{-1}$	Mass-specific backscattering coefficient of particulate matter
<i>Apparent Optical Properties (AOPs)</i>		
R_{rs}	sr^{-1}	Above-water remote sensing reflectance at 0^+
r_{rs}	sr^{-1}	Subsurface remote sensing reflectance at 0^-
<i>Ancillary Physical Variables</i>		
T	$^{\circ}\text{C}$	Water temperature
S	–	Water salinity

2. Study sites and datasets

2.1. Study sites

This study focused on five sites located in Australian coastal waters, as shown in Fig. 1. The Fitzroy Estuary and Keppel Bay sites are located near the mouth of Fitzroy River, Queensland, with the former situated inside the estuary and the latter downstream in open coastal waters in Keppel Bay. The Boston Bay site is located in the strait between Boston Island and the mainland town of Port Lincoln, within Boston Bay in Spencer Gulf, South Australia. The Cockburn Sound site is located within Cockburn Sound, Western Australia, between Garden Island and the Perth metropolitan coast. The last site, Lucinda Jetty, is located in the coastal waters of the Great Barrier Reef World Heritage Area, close to the Herbert River Estuary and the Hinchinbrook Channel in Queensland. These geographically distinct sites cover several climatic zones, including tropical, subtropical, and temperate climates, and are influenced to varying degrees by terrestrial freshwater discharge from rivers, as summarised in Table 2.

Table 2: Five experimental sites in Australian coastal waters used for biogeochemical parameter retrieval from near-surface hyperspectral remote sensing reflectance (R_{rs}) observations.

Site name	State	Nominal geo-coordinates	Climate zone	River influence
Fitzroy Estuary	Queensland	23°30'07"S, 150°48'03"E	Subtropical	High
Keppel Bay	Queensland	23°27'54"S, 150°56'39"E	Subtropical	Moderate
Boston Bay	South Australia	34°43'03"S, 135°54'02"E	Temperate	None
Cockburn Sound	Western Australia	32°15'03"S, 115°43'42"E	Temperate	Low
Lucinda Jetty	Queensland	18°31'11"S, 146°23'10"E	Tropical	Moderate

2.2. Near-surface hyperspectral R_{rs} observations

A HydraSpectra instrument (Fig. 2a) was deployed to measure hyperspectral water-leaving R_{rs} at each of the Fitzroy Estuary, Keppel Bay, Boston Bay, and Cockburn Sound sites. These instruments were calibrated in the laboratory prior to deployment. It operated autonomously, powered by a solar-recharged battery, and recorded hyperspectral data at 15-minute intervals. The recorded spectral measurements include downwelling solar irradiance ($E_d(\lambda)$), upwelling water-leaving radiance ($L_w(\lambda)$), and diffuse skylight radiance ($L_{sky}(\lambda)$). These measurements were used to calculate the water-leaving R_{rs} following the method described in Mobley (1999). To ensure a high signal-to-noise ratio for the HydraSpectra sensor, we selected R_{rs} observations acquired around local noontime, when solar irradiance is usually stronger than at other times of the day, for our analysis. Built

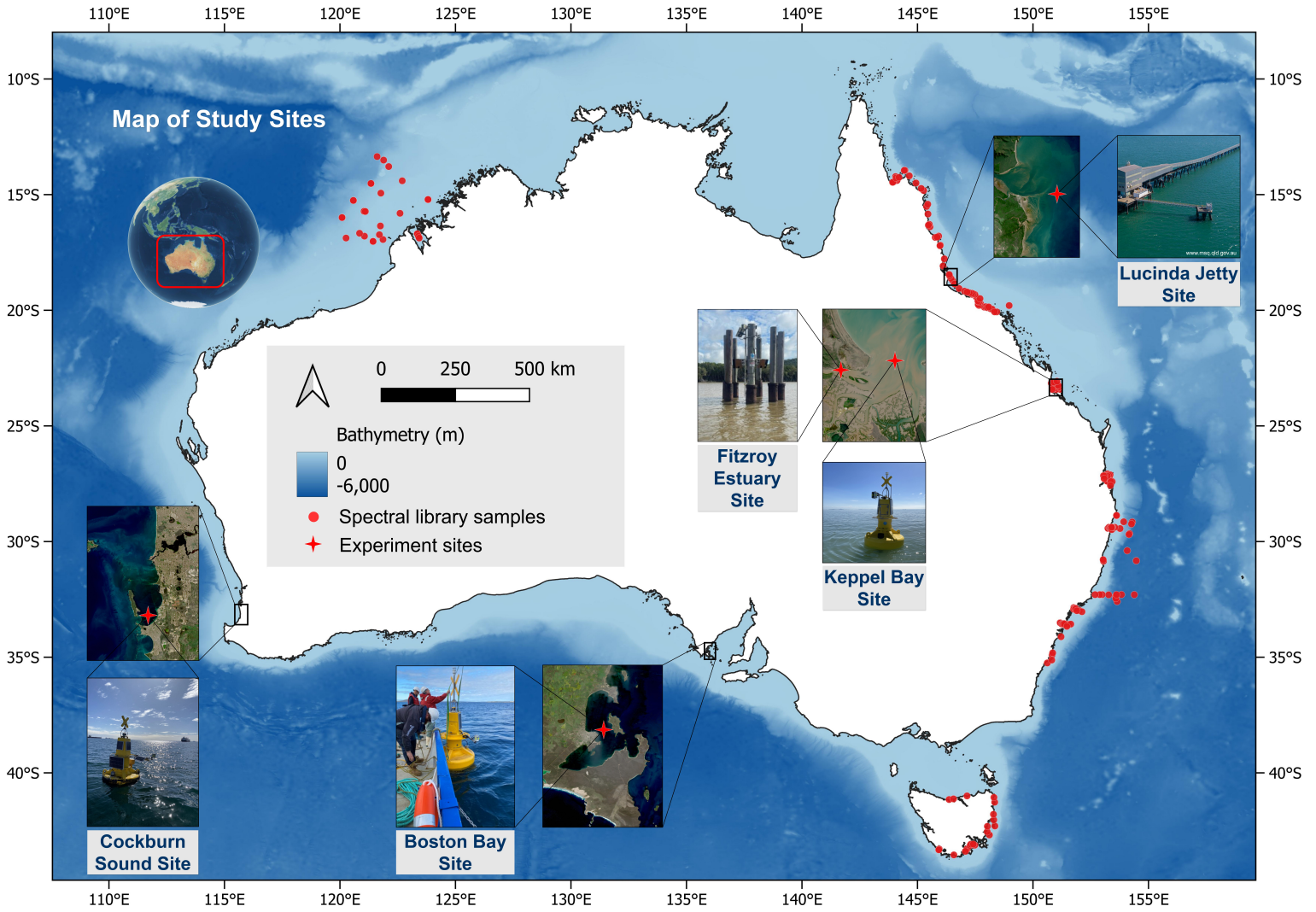


Figure 1: This study was conducted across five experimental sites in Australian coastal waters: Fitzroy Estuary, Keppel Bay, Boston Bay, Cockburn Sound, and Lucinda Jetty. The map also shows the locations (red dot points) where the bio-optical spectral library samples were collected. Insets show satellite images of the experimental sites and adjacent areas, along with photos of the instruments taken during or after deployment.

into the HydraSpectra instrument, two RGB cameras operated concurrently with the spectral sensors to capture true-colour images of the hemispherical sky and the water horizon. These images were reviewed by a technician during the Quality Assurance and Quality Control (QA/QC) process to identify and exclude low-quality R_{rs} observations, such as those affected by sun glint, bad weather, or wildlife interference. Only high-fidelity spectra were retained for analysis. Each R_{rs} spectrum spanned over the spectral range of 400–700 nm, with a spectral resolution of approximately 3 nm and a sampling interval of 1 nm. Data outside this range were excluded from our analysis due to low signal-to-noise ratios. These HydraSpectra instruments were regularly serviced and calibrated by the CSIRO servicing team. At the Lucinda Jetty site, water-leaving hyperspectral R_{rs} was derived from measurements acquired using a Hyperspectral Ocean Colour Radiometer (HyperOCR). These data

are available through the Integrated Marine Observing System (IMOS) via the Australian Ocean Data Network (AODN) portal². Similar to the HydraSpectra data, the spectral range from 400 to 700 nm in the HyperOCR measurements was used for analysis.

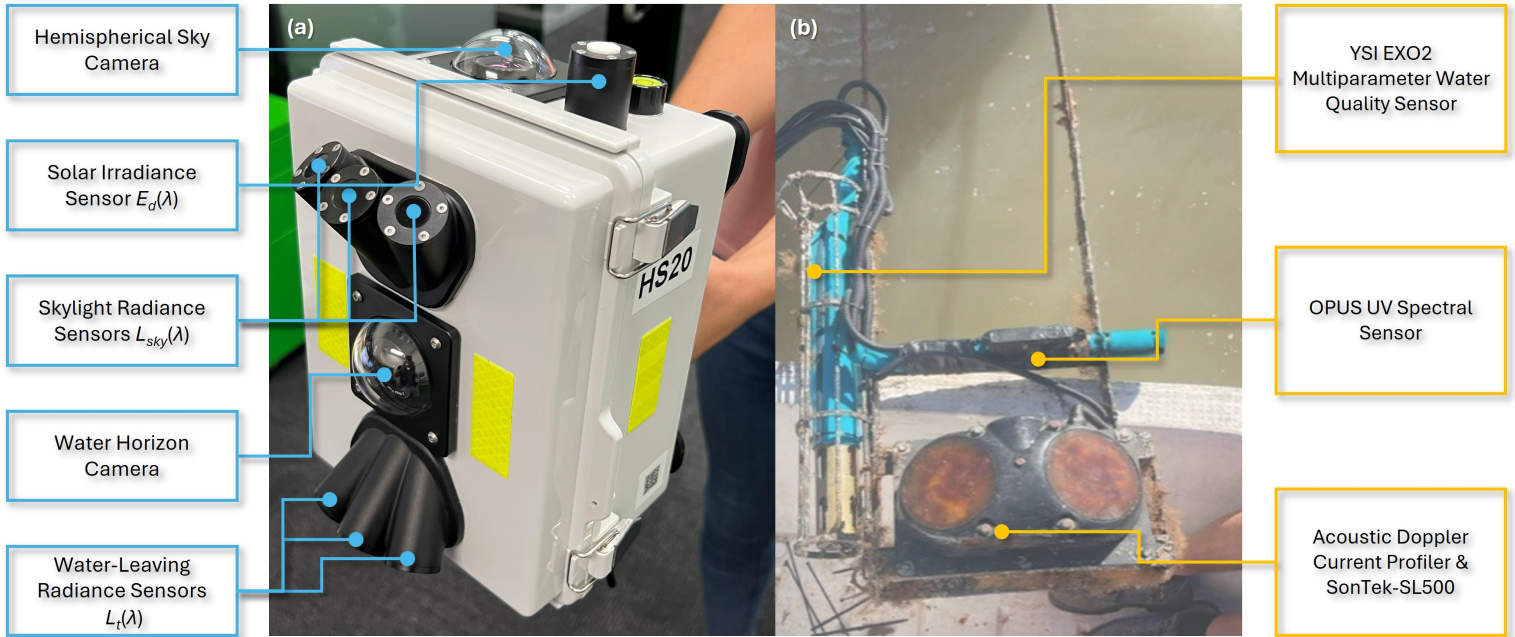


Figure 2: In situ sensors deployed at the experimental sites of Fitzroy Estuary, Keppel Bay, Boston Bay, and Cockburn Sound. (a) HydraSpectra instrument for recording water-leaving hyperspectral remote sensing reflectance (R_{rs}). (b) In-water sensors for collecting biogeochemical measurements and monitoring water conditions.

2.3. In situ BGC parameter measurements

At the experimental sites of Fitzroy Estuary, Keppel Bay, Boston Bay, and Cockburn Sound, a YSI EXO2 multiparameter sonde and an OPUS UV Spectral Sensor (Fig. 2b) were installed at a nominal depth of 1 m below the water surface, at the same location as the above-water HydraSpectra deployment. Both sensors were configured to record BGC measurements at 10 min intervals. To ensure data quality, these sensors underwent regular servicing during the study period. In cases of malfunction, emergency repairs were performed soonest possible to minimise data interruptions. For the Lucinda Jetty site, grab samples of water were collected at the same location as the above-water HyperOCR deployment, and are available through the IMOS AODN portal³. The number of in situ BGC samples and the corresponding sampling period at each experimental site are listed in Table 3.

²<https://thredds.aodn.org.au/thredds/catalog/IMOS/SRS/OC/LJCO/HyperOCR-hourly/catalog.html>

³<https://thredds.aodn.org.au/thredds/catalog/IMOS/SRS/OC/BODBAW/catalog.html>

Table 3: Summary of in situ biogeochemical samples collected at each experimental site, including the number of samples and the corresponding sampling periods.

Site	No. of Samples	Sampling Period
Fitzroy Estuary	296	26 April 2023 – 23 September 2024
Keppel Bay	377	1 June 2023 – 28 November 2024
Boston Bay	774	1 September 2022 – 2 February 2025
Cockburn Sound	172	15 July 2023 – 18 February 2024
Lucinda Jetty	104	12 November 2019 – 1 November 2023

2.4. Bio-optical spectral library

We compiled a bio-optical spectral library using 247 in situ bio-optical samples collected from several regions along Australia’s coastline, including coastal waters in Queensland, New South Wales, Tasmania, and Western Australia, as shown in Fig. 1. These in situ bio-optical measurements cover a wide range of optical water types and hydro-optical conditions with broad representativeness of Australian coastal waters. The library is built upon multiple field campaigns conducted between 2002 and 2022, including: (1) seven voyages in the inshore estuarine, lagoonal, and reef waters of the Great Barrier Reef during four dry and one wet tropical seasons between October 2002 and September 2005 (Oubelkheir et al., 2006; Blondeau-Patissier et al., 2009); (2) a voyage in Tasmanian coastal waters from 21 to 30 May 2007 (Cherukuru et al., 2014); (3) a voyage in the western Tasman Sea, off the New South Wales coast, conducted from 15 to 30 October 2010 (Cherukuru et al., 2016a); (4) a voyage across the Kimberley shelf off northwest Western Australia from 14 April to 5 May 2010 (Cherukuru et al., 2019); (5) five voyages in Moreton Bay, Queensland, in 2011 following a major flood event (Oubelkheir et al., 2014); (6) a voyage in Princess Charlotte Bay, Queensland, conducted from 30 January to 1 February 2013 after the passage of Tropical Cyclone Oswald (Oubelkheir et al., 2023); and (7) two voyages across three estuaries along the New South Wales coast in March and July 2022, respectively (Unnithan et al., 2025).

For each water sample in the bio-optical library, the following BGC parameters, IOPs, and ancillary physical variables were measured: (1) water temperature (in unit of °C), (2) water salinity (unitless), (3) TSS (in unit of mg/L), (4) TChl-a (in unit of $\mu\text{g/L}$), (5) DOC (in unit of mg/L), (6) absorption coefficient of CDOM at 440 nm ($a_y(\lambda_{440})$, in unit of m^{-1}) and its spectral slope ($S_y(\lambda_{440})$, in unit of nm^{-1}), (7) backscattering coefficient of particulate matter at 550 nm ($b_{bp}(\lambda_{550})$, in unit of m^{-1}) and its spectral slope ($S_{bbp}(\lambda_{550})$, unitless), (8) absorption coefficient of particulate matter within 400–700 nm ($a_p(\lambda)$, in unit of m^{-1}), (9) absorption coefficient of NAP within 400–700 nm ($a_d(\lambda)$, in unit of m^{-1}), and (10) absorption coefficient of phytoplankton within 400–700 nm

($a_{ph}(\lambda)$, in unit of m^{-1}).

The SIOPs were then derived as follows. The mass-specific absorption coefficient of CDOM ($a_y^*(\lambda)$, in unit of $\text{m}^2 \text{g}^{-1}$) was derived as:

$$a_y^*(\lambda) = a_y(\lambda_{440}) \times \exp[-S_y(\lambda_{440}) \times (\lambda - \lambda_{440})] / \text{DOC}. \quad (1)$$

The mass-specific backscattering coefficient of particulate matter ($bb_p^*(\lambda)$, in unit of $\text{m}^2 \text{g}^{-1}$) was derived as:

$$b_{bp}^*(\lambda) = b_{bp}(\lambda_{550}) \times (\lambda / \lambda_{550})^{-S_{bbp}(\lambda_{550})} / \text{TSS}. \quad (2)$$

The mass-specific absorption coefficient of NAP ($a_d^*(\lambda)$, in unit of $\text{m}^2 \text{g}^{-1}$) was calculated as:

$$a_d^*(\lambda) = a_d(\lambda) / \text{TSS}. \quad (3)$$

The mass-specific absorption coefficient of phytoplankton ($a_{ph}^*(\lambda)$, in unit of $\text{m}^2 \text{mg}^{-1}$) was calculated as:

$$a_{ph}^*(\lambda) = a_{ph}(\lambda) / \text{TChl-a}. \quad (4)$$

3. Methods

3.1. Overview

In this study, we aim to develop a region-adaptable approach for retrieving BGC parameters from in situ hyperspectral R_{rs} measurements. Given that the relationship between R_{rs} and BGC parameters may vary from one region to another due to distinct regional bio-optical characteristics, we propose a two-stage framework for model training, as shown in Fig. 3. In the first stage, a physics-based bio-optical forward model was adopted to simulate a large synthetic dataset linking BGC parameters and their SIOPs with hyperspectral R_{rs} . The simulation was conducted based on the bio-optical spectral library (as introduced in Subsection 2.4). Then, a region-agnostic base model was trained with the synthetic dataset using meta-learning. In the second stage, the base model was fine-tuned for each target region using in situ BGC- R_{rs} samples (as detailed in Subsections 2.2 and 2.3), resulting in a region-specific model for each region. These region-specific models were adapted from the pretrained base model rather than trained from scratch, potentially alleviating the amount of required in situ samples from each region. This two-stage framework was designed to integrate physical modelling with data-driven learning, with the potential to accommodate regional bio-optical distinctions and reduce the need for large region-specific collections of in situ samples. The proposed framework is described in detail in the subsequent Subsections.

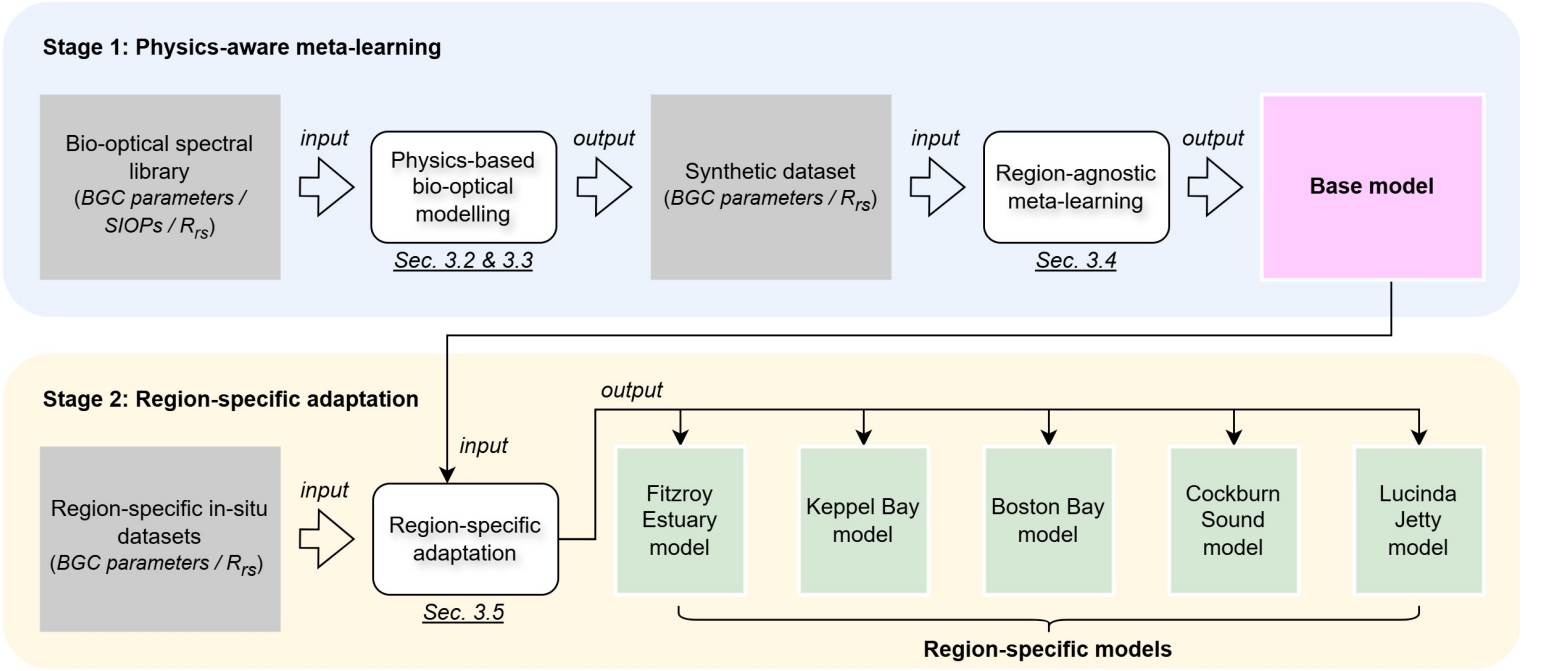


Figure 3: Flowchart of the proposed physics-aware meta-learning approach for hyperspectral retrieval of bio-geochemical parameters. It consists of two major stages: (1) a physics-aware pretraining stage (detailed in Subsections 3.2, 3.3, and 3.4), and (2) a region-specific adaptation stage (detailed in Subsection 3.5). Please refer to the nomenclature in Table 1 for definitions of symbols and acronyms.

3.2. Bio-optical forward model

We use a physics-based bio-optical model to link BGC parameters and their SIOPs with hyperspectral R_{rs} . Specifically, the total absorption coefficient of the water column, a , is expressed as:

$$a(\lambda, T, S) = a_w(\lambda, T, S) + \text{TSS} \times a_d^*(\lambda) + \text{DOC} \times a_y^*(\lambda) + \text{TChl-a} \times a_{ph}^*(\lambda), \quad (5)$$

where a_w is the absorption coefficient of water; a_d^* , a_y^* , and a_{ph}^* are mass-specific absorption coefficients of NAP, CDOM, and phytoplankton, respectively. Given that most of our experimental sites are located in coastal waters influenced by freshwater–seawater mixing, the spectral curve of a_w is computed accounting for variations in water salinity (S) and temperature (T) to enhance accuracy:

$$a_w(\lambda, T, S) = a_w^{\text{ref}}(\lambda) + (T - T_w^{\text{ref}}) \times \Psi_T(\lambda) + S \times \Psi_S(\lambda), \quad (6)$$

where a_w^{ref} is the reference water absorption spectrum, adapted from Pope and Fry (1997); $T_w^{\text{ref}} = 22^\circ\text{C}$ is the reference temperature; Ψ_T and Ψ_S are the correction coefficients for temperature and salinity, respectively, adapted from Röttgers et al. (2014).

The backscattering coefficient, b_b , is calculated as:

$$b_b(\lambda, S) = b_{bw}(\lambda, S) + \text{TSS} \times b_{bp}^*(\lambda), \quad (7)$$

where b_{bp}^* is the mass-specific backscattering coefficient of particulate matter; b_{bw} , which is the backscattering coefficient of water that depends primarily on wavelength (λ) and salinity (S), is calculated using the formula given by Boss and Pegau (2001):

$$b_{bw}(\lambda, S) = 1.38 \times (\lambda/500)^{-4.32} \times (1 + 0.3 \times S/37) \times 10^{-4}. \quad (8)$$

Following a standard radiative-transfer approximation (Lee et al., 2002), the subsurface R_{rs} at 0^- , r_{rs} , is related to the total backscattering albedo, u , by:

$$r_{rs}(\lambda) = g_0 \times u(\lambda) + g_1 \times u^2(\lambda), \quad (9)$$

where $g_0 = 0.082$ and $g_1 = 0.17$ are empirical coefficients derived from the HydroLight radiative transfer model (Mobley, 1989), and u is expressed as:

$$u(\lambda) = \frac{b_b(\lambda)}{a(\lambda) + b_b(\lambda)}. \quad (10)$$

To obtain the above-water R_{rs} at 0^+ , R_{rs} , we apply a standard air–water interface correction:

$$R_{rs}(\lambda) = \frac{0.52 \times r_{rs}(\lambda)}{1 - 1.7 \times r_{rs}(\lambda)}. \quad (11)$$

where the correction coefficients 0.52 and 1.7 follow the values given in Lee et al. (2002).

3.3. Synthetic data generation

We generate a physics-based synthetic dataset with bio-optical modelling. The bio-optical forward model, as described in Subsection 3.2, takes TSS, DOC, TChl-a, a_d^* , a_y^* , a_{ph}^* , b_{bp}^* , T , and S as inputs, and produces the water-leaving R_{rs} . For any given set of input values, the model is able to simulate the corresponding hyperspectral R_{rs} . Randomly selected sets of input values may result in physically unrealistic simulations. To enable physically consistent and plausible simulations, the values for simulation inputs are sampled with the help of the bio-optical spectral library, as introduced in Subsection 2.4, which comprises 247 in situ bio-optical measurements with broad representativeness of Australian coastal waters. Specifically, we first characterise the statistical distribution of the spectral library measurements and then draw simulation inputs from this distribution, aiming to align the sampled values with the observed measurements. These sampled simulation inputs are subsequently passed to the bio-optical forward model to generate the synthetic hyperspectral R_{rs} . This procedure is detailed in the following paragraphs.

We first apply two preprocessing steps to the spectral library measurements before modelling their statistical distribution. The first step is to transform the values of TSS, DOC, TChl-a, a_d^* , a_y^* , a_{ph}^* , and b_{bp}^* into the \log_{10} scale. Because the spectral library measurements of these BGC parameters and SIOPs are skewed towards small values, \log_{10} -scaling helps normalise their distributions and stabilise subsequent modelling, as recommended by

Seegers et al. (2018). We denote the \log_{10} -scaled TSS, DOC, and TChl-a as $\mathbf{x}_{\text{TSS}}, \mathbf{x}_{\text{DOC}}, \mathbf{x}_{\text{TChl-a}} \in \mathbb{R}^N$, where $N = 247$ is the number of spectral library measurements. Similarly, the \log_{10} -scaled a_d^* , a_y^* , a_{ph}^* , and b_{bp}^* are denoted as $\mathbf{A}_d, \mathbf{A}_y, \mathbf{A}_{ph}, \mathbf{B}_{bp} \in \mathbb{R}^{M \times N}$, with $M = 301$ spectral bands covering 400–700 nm with a 1 nm interval. The T and S measurements are not strongly skewed and therefore left unscaled, and are denoted as $\mathbf{x}_T, \mathbf{x}_S \in \mathbb{R}^N$.

The second preprocessing step is to handle the spectral dependency of a_d^* , a_y^* , a_{ph}^* , and b_{bp}^* . Unlike other input variables to the bio-optical forward model, these SIOPs are wavelength-dependent. For each of these variables, the values across adjacent wavelengths are highly correlated, forming smooth and continuous spectral shapes in nature. To preserve these correlations across wavelengths, we transform a_d^* , a_y^* , a_{ph}^* , and b_{bp}^* using the following procedure, taking a_d^* as an example. We first transform \mathbf{A}_d , which collects \log_{10} -scaled a_d^* measurements from the spectral library, from the original spectral space into a principal component (PC) space using principal component analysis (PCA). Specifically, we first mean-centre \mathbf{A}_d , and then apply singular value decomposition (SVD) to the mean-centred matrix $\bar{\mathbf{A}}_d$:

$$\bar{\mathbf{A}}_d = \mathbf{U}\mathbf{S}\mathbf{V}^\top. \quad (12)$$

where $\mathbf{U} \in \mathbb{R}^{M \times M}$ contains the PCs of $\bar{\mathbf{A}}_d$. As a property of SVD, the first few PCs represent mostly the information of spectral variance, while the last few record mainly negligible residual variance and noise (Deisenroth et al., 2020). As a balance between information preservation and noise reduction, we use the first P PCs, $\mathbf{U}_P \in \mathbb{R}^{M \times P}$, with P being set to 5 in this study, to provide a representation of $\bar{\mathbf{A}}_d$ in the PC space. The corresponding PCA scores are thus computed as:

$$\mathbf{X}_d = \mathbf{U}_P^\top \bar{\mathbf{A}}_d, \quad (13)$$

where $\mathbf{X}_d \in \mathbb{R}^{P \times N}$ is PC scores for the N spectral library measurements of a_d^* . The PCA transformation is also applied to \mathbf{A}_y , \mathbf{A}_{ph} , and \mathbf{B}_{bp} , which collect the \log_{10} -scaled measurements of a_y^* , a_{ph}^* , and b_{bp}^* in the spectral library, respectively. The transformed data are represented in the PC space as \mathbf{X}_y , \mathbf{X}_{ph} , and \mathbf{X}_{bbp} . This transformation captures the dominant modes of spectral variability while preserving the correlations across wavelengths, as the spectral shapes are represented by a compact set of uncorrelated PCs.

We then model the joint statistical distribution of TSS, DOC, TChl-a, a_d^* , a_y^* , a_{ph}^* , b_{bp}^* , T , and S in the bio-optical spectral library based on their preprocessed values. Two considerations motivate our choice of the specific method for distribution modelling. First, while univariate models can capture the distribution of individual variables, they fail to account for the inter-correlations among variables. Second, the distributions of these variables are often non-Gaussian and may not be adequately described by a single Gaussian or a finite mixture of Gaussians. Therefore, we adopt an infinite Gaussian mixture model called the Dirichlet Process Bayesian Gaussian Mixture Model (DP-GMM), which is a non-parametric Bayesian framework suitable for modelling non-Gaussian multivariate distributions. Specifically, we first collate the preprocessed input variables

as $\mathbf{Y} \in \mathbb{R}^{(5+4 \times P) \times N}$:

$$\mathbf{Y} = \left[\mathbf{x}_{\text{TSS}}, \mathbf{x}_{\text{DOC}}, \mathbf{x}_{\text{TChl-a}}, \mathbf{X}_d, \mathbf{X}_y, \mathbf{X}_{ph}, \mathbf{X}_{bp}, \mathbf{x}_T, \mathbf{x}_S \right]^\top \quad (14)$$

Let $\mathbf{y}_n \in \mathbb{R}^{(5+4 \times P)}$ denote the n -th measurement in \mathbf{Y} , and let $\mathbf{y} \in \mathbb{R}^{(5+4 \times P)}$ denote a generic measurement. We then use DP-GMM to model the distribution of \mathbf{y} , $p(\mathbf{y})$, as an unbounded mixture of Gaussian components:

$$p(\mathbf{y}) = \sum_{i=1}^{\infty} \pi_i \mathcal{N}(\mathbf{y} \mid \boldsymbol{\mu}_i, \boldsymbol{\Sigma}_i). \quad (15)$$

where $\mathcal{N}(\cdot)$ denotes the multivariate Gaussian distribution; π_i , $\boldsymbol{\mu}_i$, and $\boldsymbol{\Sigma}_i$ are learnable parameters denoting the mixture weight, mean vector, and covariance matrix of the i -th Gaussian component, respectively.

The joint distribution $p(\mathbf{y})$ given in Eq. (15) is derived from a large number of in situ measurements in the spectral library, and thus serves as a realistic representation of the distribution and inter-correlations of BGC parameters and their SIOPs. We draw a total of K samples from $p(\mathbf{y})$ to obtain physically plausible inputs for bio-optical modelling:

$$\{\mathbf{y}^{(k)}\}_{k=1}^K \sim p(\mathbf{y}), \quad (16)$$

where $\mathbf{y}^{(k)}$ is the k -th sample drawn from the distribution, consisting of a set of parameters, including the \log_{10} -scaled TSS, DOC, and TChl-a, the \log_{10} -scaled and PCA-transformed a_d^* , a_y^* , a_{ph}^* , b_{bp}^* , and T and S . These parameters are then scaled and transformed back to their original scales and spaces, and denoted as $\text{TSS}^{(k)}$, $\text{DOC}^{(k)}$, $\text{TChl-a}^{(k)}$, $a_d^{*(k)}$, $a_y^{*(k)}$, $a_{ph}^{*(k)}$, $b_{bp}^{*(k)}$, $T^{(k)}$, and $S^{(k)}$. For each drawn sample, we input them into the bio-optical forward model and simulate the corresponding R_{rs} :

$$R_{rs}^{(k)} = f \left(\text{TSS}^{(k)}, \text{DOC}^{(k)}, \text{TChl-a}^{(k)}, a_d^{*(k)}, a_y^{*(k)}, a_{ph}^{*(k)}, b_{bp}^{*(k)}, T^{(k)}, S^{(k)} \right), \quad (17)$$

where $f(\cdot)$ is the bio-optical forward model as described in Subsection 3.2. To adequately cover the distribution of the bio-optical variables, we sampled $K = 10,000$ instances. Based on empirical test runs, this sample size was found to provide sufficient coverage of the parameter space, with larger sample sizes yielding only marginal gains for pretraining the base model. For each sample, the corresponding R_{rs} was simulated, resulting in a synthetic dataset \mathcal{D} that links BGC parameters with R_{rs} :

$$\mathcal{D} = \left\{ \left(\text{TSS}^{(k)}, \text{DOC}^{(k)}, \text{TChl-a}^{(k)}, a_d^{*(k)}, a_y^{*(k)}, a_{ph}^{*(k)}, b_{bp}^{*(k)}, T^{(k)}, S^{(k)}, R_{rs}^{(k)} \right) \right\}_{k=1}^K. \quad (18)$$

3.4. Pretraining of the base model

We pretrain a region-agnostic base model with the synthetic dataset \mathcal{D} generated in Subsection 3.3. We formulate the pretraining of the base model as a meta-learning problem and develop an approach based on the Model-Agnostic Meta-Learning (MAML) architecture (Finn et al., 2017). The base model is pretrained on a collection of tasks, where each task is formed from a subset of synthetic samples in \mathcal{D} . As \mathcal{D} is constructed

with physics-based bio-optical modelling (Subsection 3.3), the base model is able to learn the general physical relationship linking BGC parameters and hyperspectral R_{rs} through this pretraining process. Moreover, tasks are constructed with diverse SIOP settings, enabling the base model to adapt effectively to new regions characterised by distinct SIOP conditions. The pretraining of the base model is detailed in the following.

We denote the base model as $g_{\boldsymbol{\theta}}(\cdot) : \mathbb{R}^M \rightarrow \mathbb{R}^3$ with model parameters $\boldsymbol{\theta}$, mapping a hyperspectral R_{rs} spectrum $R_{rs} \in \mathbb{R}^M$ to the BGC parameters TSS, DOC, and TChl-a. In our study, the number of spectral bands is $M = 301$, covering 400–700 nm with a 1 nm interval. We pretrain $g(\cdot)$ on a distribution of tasks $p(\mathcal{T})$ sampled from \mathcal{D} . Each task τ_i is constructed by sampling a subset $\mathcal{D}_i \subset \mathcal{D}$ of $2K_i$ samples and splitting it evenly into a support (training) set \mathcal{S}_i and a query (test) set \mathcal{Q}_i , with each having K_i samples. The experimental sites considered in this study may present distinct SIOPs, due to differences in regional biogeochemistry, such as phytoplankton community composition and physiology, suspended-particle size distributions, and CDOM sources and processing. To equip $g(\cdot)$ with the ability to adapt to different SIOP scenarios, each task τ_i is sampled in a way that its synthetic samples from \mathcal{D} share similar SIOPs. Specifically, for each task, we pick a random sample from \mathcal{D} , compute its Euclidean distances to all other samples in \mathcal{D} in term of SIOPs, and select the closest $2K_i$ ones. In this way, different tasks correspond to distinct SIOP scenarios.

The adaptation ability of the base model, $g_{\boldsymbol{\theta}}(\cdot)$, is learned by adapting its parameters to each of the sampled tasks. Here, we distinguish the parameters of the base model, $\boldsymbol{\theta}$, which serve as meta-parameters shared across all tasks, from the task-specific parameters, $\boldsymbol{\phi}_i$, which are obtained by adapting $\boldsymbol{\theta}$ to the i -th task τ_i . In other words, $\boldsymbol{\theta}$ represents the general knowledge shared across tasks, while $\boldsymbol{\phi}_i$ captures the additional task-specific knowledge learned from the particular task τ_i . For the i -th task τ_i , $\boldsymbol{\phi}_i$ are obtained by adapting $\boldsymbol{\theta}$ to the support set \mathcal{S}_i , via minimising the following loss function $\mathcal{L}_{\mathcal{S}_i}$ that measures the discrepancy between the model-predicted and the true values of TSS, DOC, and TChl-a:

$$\mathcal{L}_{\mathcal{S}_i}(\boldsymbol{\phi}_i) = \frac{1}{K_i} \sum_{(R_{rs}, [\text{TSS}, \text{DOC}, \text{TChl-a}]) \in \mathcal{S}_i} \|g_{\boldsymbol{\phi}_i}(R_{rs}) - [\text{TSS}, \text{DOC}, \text{TChl-a}]\|_2^2 \quad (19)$$

The accuracy of this adaptation is then measured on the query set with the same type of loss function $\mathcal{L}_{\mathcal{Q}_i}$. Then, the parameters of the base model, $\boldsymbol{\theta}$, are optimised by minimising the meta loss, $\mathcal{J}(\boldsymbol{\theta})$, which is expressed as the average query loss across all tasks:

$$\mathcal{J}(\boldsymbol{\theta}) = \frac{1}{B} \sum_{i=1}^B \mathcal{L}_{\mathcal{Q}_i}(\boldsymbol{\phi}_i(\boldsymbol{\theta})), \quad (20)$$

where B is the total number of tasks, and $\boldsymbol{\phi}_i(\boldsymbol{\theta})$ stands for the adapted parameters $\boldsymbol{\phi}_i$ to the i -th task τ_i under the meta-parameters $\boldsymbol{\theta}$.

An algorithmic description of the meta-learning procedure for pretraining the based model $g(\cdot)$ is given in Algorithm 1. This algorithm trains the base model by repeatedly adapting it to a collection of tasks sampled from

the physics-based synthetic dataset \mathcal{D} , each constructed with a varying number of samples and characterised by distinct SIOP characteristics. Through this process, the model learns not only the general physical relationships between hyperspectral R_{rs} and BGC parameters, but also the capacity to adapt effectively to new tasks with varying sample sizes and SIOP conditions.

Algorithm 1 Pretraining of base model with meta-learning

Inputs: Synthetic dataset \mathcal{D} , meta-parameters θ , inner learning rate α , outer learning rate β , maximum epochs

E

- 1: Sample a batch of tasks $\{\tau_i\}_{i=1}^B \sim p(\mathcal{T})$, with each task being constructed by selecting $2K_i$ nearest neighbours in SIOP space around a random centre from \mathcal{D}
- 2: **for** $e = 1$ to E **do**
- 3: **for** each task τ_i **do**
- 4: Split into support set \mathcal{S}_i and query set \mathcal{Q}_i of size K_i each
- 5: Initialise task parameters: $\phi_i \leftarrow \theta$
- 6: Compute task-specific loss $\mathcal{L}_{\mathcal{S}_i}(\phi_i)$ on \mathcal{S}_i following Eq. (19)
- 7: Update ϕ_i with gradient descent: $\phi_i \leftarrow \phi_i - \alpha \nabla_{\phi_i} \mathcal{L}_{\mathcal{S}_i}(\phi_i)$
- 8: Compute $\mathcal{L}_{\mathcal{Q}_i}(\phi_i)$ on \mathcal{Q}_i with ϕ_i analogously to Eq. (19)
- 9: **end for**
- 10: Compute meta loss $\mathcal{J}(\theta)$ on $\{\mathcal{L}_{\mathcal{Q}_i}(\phi_i)\}_{i=1}^B$ following Eq. (20)
- 11: Update θ with gradient descent: $\theta \leftarrow \theta - \beta \nabla_{\theta} \mathcal{J}(\theta)$
- 12: **end for**

Outputs: Base model $g_{\theta}(\cdot)$ with pretrained parameters θ

3.5. Region-specific model adaptation

After pretraining, the base model $g_{\theta}(\cdot)$ has learned general physical relationships linking hyperspectral R_{rs} to BGC parameters from the synthetic dataset. However, the optical properties of natural waters vary considerably among regions due to differences in constituent distributions and their IOPs/SIOPs. As a result, the pretrained base model may not fully capture the region-specific relationships between hyperspectral R_{rs} and BGC parameters. To address this, we adapt the pretrained base model to each experimental site using in situ samples collected at that site.

Let $D_r = \{(R_{rs}^{(i)}, \mathbf{y}^{(i)})\}_{i=1}^{N_r}$ denote the region-specific dataset collected from the experimental site r , where $R_{rs}^{(i)} \in \mathbb{R}^M$ represents the hyperspectral R_{rs} spectrum and $\mathbf{y}^{(i)} = [\text{TSS}, \text{DOC}, \text{TChl-a}] \in \mathbb{R}^3$ represents the corresponding BGC parameters measured in situ, with N_r denoting the number of samples available for that

site. Following the meta-learning paradigm introduced in Subsection 3.4, we treat each site as a new task and initialise the model parameters using the pretrained meta-parameters θ . The region-specific parameters ϕ_r are then obtained through iterative gradient updates using the regional dataset. Specifically, for a given set of parameters ϕ_r , the adaptation loss is defined as:

$$\mathcal{L}_r(\phi_r) = \frac{1}{N_r} \sum_{i=1}^{N_r} \|g_{\phi_r}(R_{rs}^{(i)}) - \mathbf{y}^{(i)}\|_2^2. \quad (21)$$

An algorithmic description of the procedure for region-specific model adaptation is given in Algorithm 2. This procedure iteratively adjusts the model parameters so that the predictions align with the local BGC- R_{rs} relationships observed in the target experimental site.

Algorithm 2 Region-specific model adaptation

Inputs: Pretrained base model $g_{\theta}(\cdot)$ with parameters θ , region-specific dataset \mathcal{D}_r , learning rate γ , maximum adaptation iterations I

- 1: Split \mathcal{D}_r into support set \mathcal{S}_r and query set \mathcal{Q}_r
- 2: Initialise region-specific parameters: $\phi_r \leftarrow \theta$
- 3: **for** $i = 1$ to I **do**
- 4: Compute support loss $\mathcal{L}_{\mathcal{S}_r}(\phi_r)$ on \mathcal{S}_r following Eq. (21)
- 5: Update ϕ_r with gradient descent: $\phi_r \leftarrow \phi_r - \gamma \nabla_{\phi_r} \mathcal{L}_{\mathcal{S}_r}(\phi_r)$
- 6: Compute validation loss $\mathcal{L}_{\mathcal{Q}_r}(\phi_r)$ on \mathcal{Q}_r
- 7: **end for**

Outputs: Region-specific model $g_{\phi_r}(\cdot)$ with adapted parameters ϕ_r for the experimental site r

A 10-fold cross-validation procedure was employed during adaptation to mitigate overfitting. Specifically, the dataset D_r from each experimental site was randomly partitioned into 10 approximately equal folds. Each fold was successively designated as the query set Q_r , while the remaining nine folds constituted the support set S_r . The model parameters were updated using S_r , and performance was evaluated on Q_r .

To quantitatively assess the predictive performance of the adapted model, we employed four evaluation metrics to compare the model-predicted BGC parameters derived from hyperspectral R_{rs} against in situ measurements used as ground truth. These metrics include the coefficient of determination (r^2), bias, root mean squared error (RMSE), and mean absolute error (MAE). Following the recommendations in Seegers et al. (2018), these metrics were computed in \log_{10} space to account for the skewness toward small values commonly observed in BGC parameters. The metrics are defined as follows:

$$\begin{aligned}
r^2 &= 1 - \frac{\sum_{i=1}^n (\log_{10}(y_i) - \log_{10}(\hat{y}_i))^2}{\sum_{i=1}^n \left(\log_{10}(y_i) - \overline{\log_{10}(y)} \right)^2}, \\
\text{Bias} &= 10^{\left(\frac{1}{n} \sum_{i=1}^n (\log_{10}(\hat{y}_i) - \log_{10}(y_i)) \right)}, \\
\text{RMSE} &= 10^{\sqrt{\frac{1}{n} \sum_{i=1}^n (\log_{10}(\hat{y}_i) - \log_{10}(y_i))^2}}, \\
\text{MAE} &= 10^{\left(\frac{1}{n} \sum_{i=1}^n |\log_{10}(\hat{y}_i) - \log_{10}(y_i)| \right)},
\end{aligned} \tag{22}$$

where \hat{y}_i and y_i are the model predicted and in situ measured values, respectively, and n is the total number of samples.

3.6. Accuracy assessment

The proposed approach was benchmarked against five existing models, including three empirical models and two deep-learning-based models. The empirical models are Choo et al. (2022)’s model for TSS retrieval, Cherukuru et al. (2016b)’s model for DOC retrieval, and Cherukuru et al. (2019)’s model for TChl-a retrieval. The deep-learning-based models include DL-RS (Unnithan et al., 2025), which was used for benchmarking TSS and DOC, and HyperEST (Luo et al., 2025), which was used for benchmarking TSS and TChl-a. The model architectures and output variables differ across the considered models, as summarised in Table 4.

Table 4: Comparison of model architectures and output variables across the benchmark and proposed models.

Model	Model Architecture		Output Variable		
	Pretraining	Physics-aware	TSS	DOC	TChl-a
Choo et al. (2022)	–	–	✓	–	–
Cherukuru et al. (2016b)	–	–	–	✓	–
Cherukuru et al. (2019)	–	–	–	–	✓
DL-RS (Unnithan et al., 2025)	–	✓	✓	✓	–
HyperEST (Luo et al., 2025)	✓	–	✓	–	✓
Proposed	✓	✓	✓	✓	✓

Efforts were made to ensure a fair comparison among models. The benchmark models were recalibrated or fine-tuned using the same dataset as the proposed approach. The 10-fold cross-validation scheme was applied, where nine folds were used for recalibration or fine-tuning and the remaining fold for performance evaluation in each iteration. Model hyperparameters were kept consistent wherever possible. The performance of the benchmark models was assessed and compared with the proposed approach using the metrics defined in Eq. (22).

3.7. Statistical analyses

To characterise the statistical properties of the bio-optical spectral library, statistical analyses were performed on the spectral library samples. Summary statistics, including the minimum, median, maximum, mean, and standard deviation, were calculated for the BGC parameters (TSS, DOC, and TChl-a), SIOPs ($a_y^*(\lambda_{440})$, $b_{bp}^*(\lambda_{550})$, $a_d^*(\lambda_{440})$, and $a_{ph}^*(\lambda_{440})$), and ancillary physical variables (T and S), in order to quantify the dynamic range and variability of each variable. Pearson correlation coefficients (r) were calculated for pairwise combinations of these variables in order to assess whether physically meaningful inter-parameter correlations were preserved in the spectral library. In addition, chromaticity coordinates were derived from hyperspectral R_{rs} (400–700 nm) using the CIE 1931 2° standard observer under D65 illumination to assess the distribution of water colours represented in the spectral library. These analyses were used to evaluate the representativeness, physical consistency, and optical diversity of the spectral library.

A global sensitivity analysis was performed on the bio-optical forward model using the Extended Fourier Amplitude Sensitivity Test (EFAST) (Saltelli et al., 1999) to quantify the relative contributions of TSS, DOC, and TChl-a to variations in model-simulated hyperspectral R_{rs} across the 400–700 nm spectral range. We computed first-order sensitivity indices to quantify the direct effect of each variable to the model output, and total sensitivity indices to quantify the overall contribution of each variable, including both its direct effect and its interaction effects with other variables. Similar procedures have been applied in prior studies to assess the sensitivities of other physics-based hyperspectral models (*e.g.*, Zhao et al. (2014a,b)). This analysis aimed to identify the dominant spectral regions influenced by each BGC parameter and provide a quantitative assessment of the physical plausibility of the bio-optical forward model.

To evaluate whether the synthetic dataset generated via the bio-optical forward model preserves the statistical characteristics of the in situ spectral library, distributional and correlation-based comparisons were conducted. Histograms were used to compare the marginal distributions of TSS, DOC, and TChl-a between synthetic and measured samples. Spectral comparisons were performed to assess whether synthetic SIOP spectra (a_d^* , a_y^* , a_{ph}^* , and b_{bp}^*) and simulated R_{rs} preserved realistic spectral smoothness and characteristic absorption features. The Kolmogorov–Smirnov (KS) test was applied to quantitatively assess if there is a significant difference between the distributions of synthetic and observed samples, with significance evaluated at the $p=0.05$ level. Furthermore, joint distributions of selected parameter pairs were examined, and Pearson correlation coefficients were compared between synthetic and spectral library samples to assess whether inter-parameter dependencies were maintained. These analyses aimed to ensure that the synthetic dataset not only reproduced marginal distributions but also preserved multivariate statistical structure and physical relationships present in the in situ data.

To characterise regional variability among the experimental sites, time-series analyses of R_{rs} and BGC parameters were conducted. Model-predicted BGC concentrations derived from R_{rs} were compared with con-

current in situ measurements to assess consistency in magnitude and temporal dynamics. Spectral variability was examined by analysing both R_{rs} magnitude and peak wavelength positions across sites. To further evaluate inter-site distinctions, the distribution of BGC parameters was analysed, and apparent water colours were quantified by transforming R_{rs} spectra into the International Commission on Illumination (CIE) 1931 chromaticity coordinates. These analyses aimed to analyse regional distinctions among the experimental sites.

4. Results and Discussions

4.1. Analysis of the bio-optical spectral library

The statistical characteristics of the BGC parameters, SIOPs, and ancillary physical variables in the bio-optical spectral library, which consists of a total of 247 in situ samples, are summarised in Table 5, including the minimum, median, maximum, mean, and standard deviation for each variable. As shown in the table, the spectral library covers a broad dynamic range for each BGC parameter, SIOP, and ancillary physical variable. In particular, the samples extend from near-freshwater conditions (0.08) to fully marine salinities (39.4), and from relatively cool (12.1 °C) to warm waters (31.4 °C). This indicates that the spectral library encompasses a wide range of environmental conditions representative of both river-affected estuarine and open-ocean waters. The broad representativeness of the spectral library samples provides a basis to guide the pretraining of the base model, allowing it to learn generalised BGC- R_{rs} relationships across diverse water types and environmental conditions.

Fig. 4 presents the Pearson correlation matrix for the measurements in the bio-optical spectral library. The coefficients of correlation (r) were computed for all pairwise combinations of T , S , TSS, DOC, TChl-a, $a_y(\lambda_{440})$, $b_{bp}(\lambda_{550})$, $a_d(\lambda_{440})$, and $a_{ph}(\lambda_{440})$. It was found that water temperature T exhibits weak correlations with BGC parameters and IOPs with $|r| \leq 0.08$, which is expected since water constituents are primarily governed by hydrological inputs and transport processes rather than by temperature itself. In contrast, water salinity S is generally negatively correlated with BGC parameters and IOPs with r ranging between -0.72 to -0.57 , as freshwater inflows both reduce seawater salinity and concurrently introduce elevated loads of particulates and dissolved matter from terrestrial sources. TSS exhibits strong correlations with particulate IOPs: it is highly correlated with the particulate backscattering coefficient at 550 nm ($b_{bp}(\lambda_{550})$) with $r = 0.84$, NAP absorption coefficient at 440 nm ($a_d(\lambda_{440})$) with $r = 0.90$, and phytoplankton absorption coefficient at 440 nm ($a_{ph}(\lambda_{440})$) with $r = 0.78$. This is physically consistent, as TSS represents the concentration of suspended particulate matter, encompassing both inorganic NAP and organic phytoplankton components, and therefore influences both light scattering and particulate absorption. DOC shows a strong positive correlation with CDOM absorption at 440 nm ($a_y(\lambda_{440})$) with $r = 0.72$. This relationship is expected because DOC is closely associated with CDOM

Table 5: Minimum, median, maximum, mean, and standard deviation values of the biogeochemical parameters, specific inherent optical properties, and ancillary physical variables in the bio-optical spectral library. Please refer to the nomenclature in Table 1 for definitions of symbols and acronyms.

Parameter	Minimum	Median	Maximum	Mean \pm Standard Deviation
T ($^{\circ}\text{C}$)	12.1278	25.1900	31.4035	24.3005 ± 5.1366
S (-)	0.0800	33.4200	39.4000	28.3883 ± 9.8507
TSS (mg/L)	0.1333	2.6000	69.8300	6.8920 ± 10.6366
DOC (mg/L)	0.2400	1.3000	14.2500	2.1774 ± 2.1996
TChl-a ($\mu\text{g/L}$)	0.0589	0.9627	22.0372	2.2042 ± 3.3301
$a_y^*(\lambda_{440})$ ($\text{m}^2 \text{g}^{-1}$)	0.0037	0.2302	2.5521	0.3074 ± 0.2882
$b_{bp}^*(\lambda_{550})$ ($\text{m}^2 \text{g}^{-1}$)	0.0001	0.0077	0.0416	0.0081 ± 0.0059
$a_d^*(\lambda_{440})$ ($\text{m}^2 \text{g}^{-1}$)	0.0018	0.0305	0.2573	0.0369 ± 0.0306
$a_{ph}^*(\lambda_{440})$ ($\text{m}^2 \text{mg}^{-1}$)	0.0099	0.0591	0.4004	0.0763 ± 0.0599

concentration, which highly affects light absorption in the blue spectral region. TChl-a shows reasonably strong correlation with phytoplankton absorption at 440 nm ($a_{ph}(440)$) with $r = 0.88$, reflecting the dependence of phytoplankton absorption on chlorophyll concentration. The results of this correlation analysis indicate that the underlying physical correlations among variables are well preserved in the spectral library measurements.

The CIE 1931 chromaticity diagram in Fig. 5 shows the colour distribution of in situ samples in the bio-optical spectral library. The chromaticity coordinates of spectral library samples were derived from their R_{rs} spectra (400–700 nm) using the CIE 1931 2° standard observer under D65 illumination. The distribution of these samples follows a trajectory that closely resembles the chromaticity progression of the Forel–Ule (FU) colour scale (*e.g.*, Wernand and Van der Woerd (2010); Novoa et al. (2013)), and spans the FU range from blue and green to yellow and brown waters. It was also observed from that figure that salinity exhibits a systematic gradient along the chromaticity trajectory, with lower-salinity samples generally associated with greener to bluer colours, and higher-salinity samples tending towards yellower to browner colours. These findings indicate that the bio-optical spectral library employed in this study provides a representative coverage of diverse water colours.

4.2. Analysis of the bio-optical forward model

Fig. 6 shows the wavelength-dependent first-order and total sensitivity indices of the bio-optical forward model parameters of TSS, DOC, and TChl-a, derived using the EFAST analysis (Saltelli et al., 1999) across the 400–700 nm spectral range. TSS exhibits progressively increasing sensitivity toward longer wavelengths,

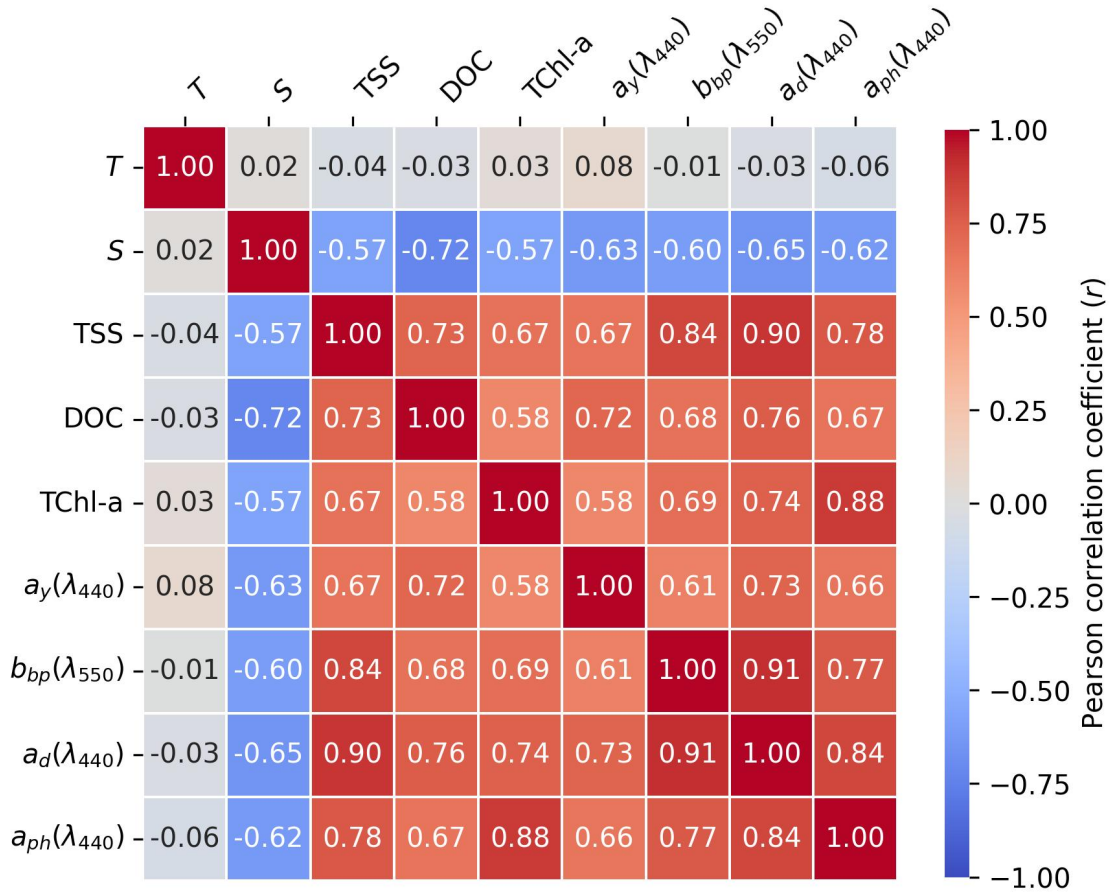


Figure 4: Pearson correlation matrix among biogeochemical parameters (TSS, DOC, and TChl-a), inherent optical properties ($a_y(\lambda_{440})$, $b_{bp}(\lambda_{550})$, $a_d(\lambda_{440})$, and $a_{ph}(\lambda_{440})$) and ancillary physical variables (T and S) for samples in the bio-optical spectral library. Please refer to the nomenclature in Table 1 for definitions of symbols and acronyms.

reflecting the high influence of particle backscattering in the red region. In contrast, DOC shows higher sensitivity in the blue domain and decreases toward the red, consistent with the relatively higher absorption of CDOM at shorter wavelengths. TChl-a displays comparatively lower overall sensitivity, with relatively higher sensitivity in the blue and near 680 nm regions corresponding to known chlorophyll absorption features in these regions. Previous studies have shown that absorption is generally more pronounced in the blue region than in the red due to CDOM and phytoplankton pigments, whereas scattering effects associated with suspended particles tend to become relatively more important at longer wavelengths (*e.g.*, Manzo et al. (2015)). Compared with these well-established spectral characteristics of BGC parameters, the sensitivity analysis results of our bio-optical forward model, as presented in Fig. 6, suggest that our model is built upon assumptions that align well with the physical properties of water constituents.

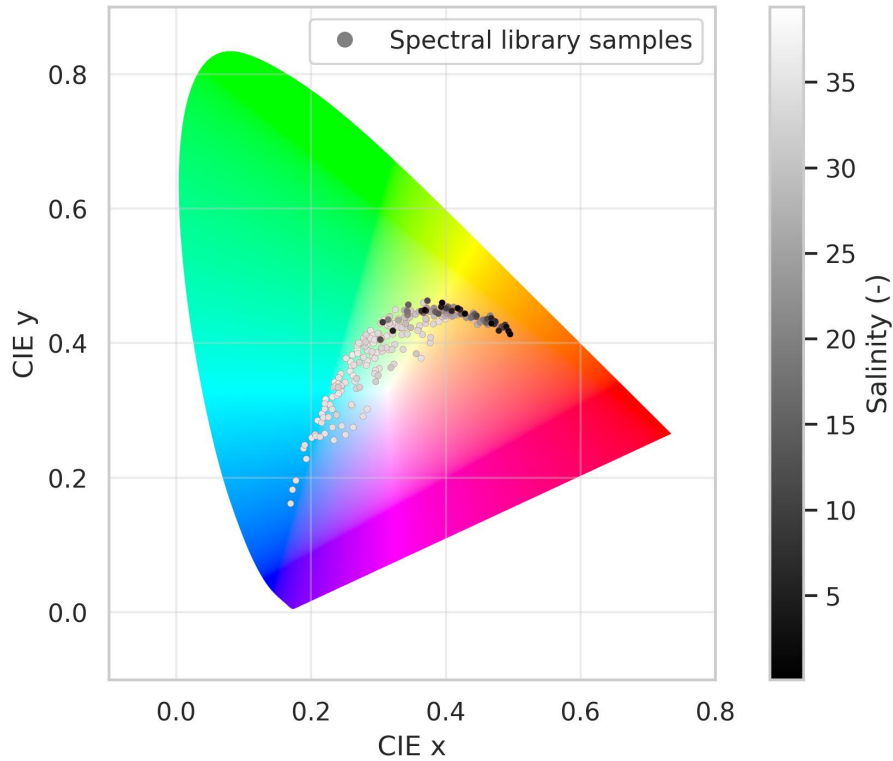


Figure 5: The International Commission on Illumination (CIE) 1931 chromaticity diagram showing the distribution of water leaving reflectance (R_{rs}) for samples in the bio-optical spectral library. Sample chromaticity coordinates were computed from the R_{rs} spectra using the CIE 1931 2° Standard Observer under CIE Standard Daylight D65 illumination. Sample points are shaded in grayscale according to their salinity.

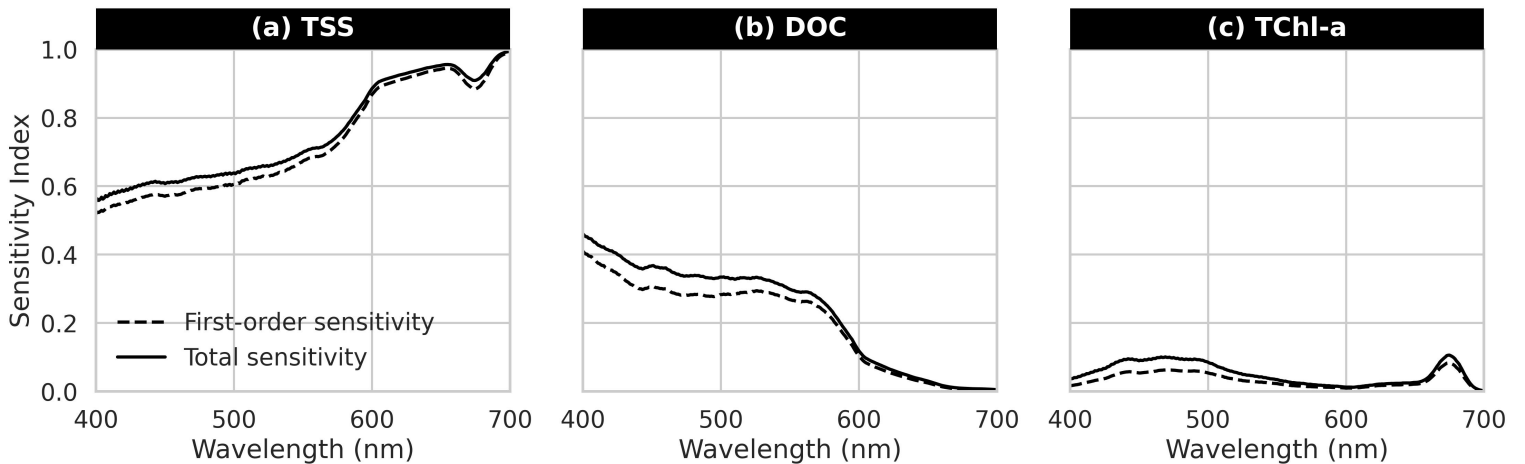


Figure 6: Wavelength-dependent first-order and total sensitivity indices derived from Extended Fourier Amplitude Sensitivity Test (EFAST) analysis (Saltelli et al., 1999) for three water quality parameters: (a) total suspended solids (TSS), (b) dissolved organic carbon (DOC), and (c) total chlorophyll-a (TChl-a) across the 400–700 nm spectral range.

4.3. Analysis of the synthetic dataset

Fig. 7 shows the distribution of 10,000 samples from the synthetic dataset \mathcal{D} in comparison with samples from the in situ spectral library. The distributions of the BGC parameters (TSS, DOC, and TChl-a) are shown in Figs. 7a–c, while the spectral shapes of the SIOPs (a_d^* , a_y^* , a_{ph}^* , and b_{bp}^*) and R_{rs} are presented in Figs. 7d–h. The histogram comparisons in Figs. 7a–c show that the BGC parameters in the synthetic dataset not only span a similar range of values as the spectral library measurements but also generally follow their distributional patterns. The spectral comparisons in Figs. 7d–j indicate that the synthetic SIOP spectra largely preserve the spectral correlations across wavelengths (*e.g.*, spectral smoothness and absorption features) observed in the spectral library measurements, and their shapes and magnitudes also generally resemble those of the measured spectra. In particular, the chlorophyll-a absorption peaks in a_{ph}^* at 430–440 nm and 665–675 nm, evident in the spectral library spectra, are well preserved in the synthetic spectra, as shown from Fig. 7f. The simulated R_{rs} spectra also closely resemble those from the spectral library, in terms of both spectral shape and magnitude, as shown in Fig. 7h.

To qualitatively compare the distribution patterns between the synthetic samples and the spectral library measurements, Kolmogorov–Smirnov (KS) tests were performed, and the results are presented in Fig. 7. It was found that the KS statistics are generally low ($KS \leq 0.2429$) with high p-values ($p \geq 0.1045$), indicating that there is no statistical difference between the distributions of synthetic samples and spectral library measurements at the $p=0.05$ significance level. This indicates that the synthetic samples effectively capture the distributional patterns of the spectral library samples, which were collected in situ from diverse coastal waters across Australia, supporting the representativeness of the synthetic dataset.

While Fig. 7 presents distributional comparisons between the synthetic and spectral library samples for individual parameters, we further assessed whether the inter-parameter correlations observed in the spectral library are preserved in the synthetic dataset. Fig. 8 presents the joint distributions of selected parameter pairs for both synthetic and spectral library samples. The figure shows that the correlation patterns between parameters are similar for the synthetic and spectral library samples. A comparison of Pearson correlation coefficients (r) indicates that, for each parameter pair, the r values are closely aligned, with differences ranging from 0.01 (Figs. 8a and f) to 0.09 (Fig. 8g). The inter-parameter correlations observed in the spectral library have been largely preserved in the synthetic dataset.

It is worth noting that the joint distributions, as presented in Fig. 8, may not always be adequately described by a standard Gaussian distribution. For example, the joint distribution of $a_y(\lambda_{440})$ and $a_{ph}(\lambda_{440})$ shown in Fig. 8i displays a highly non-Gaussian pattern. To capture such structure, we estimated probability maps with DP-DMM (Eq. 15), which is a Bayesian nonparametric estimator that accommodates non-Gaussian multivariate distributions. The background colours in Fig. 8 show these DP-GMM probability estimates, which closely track

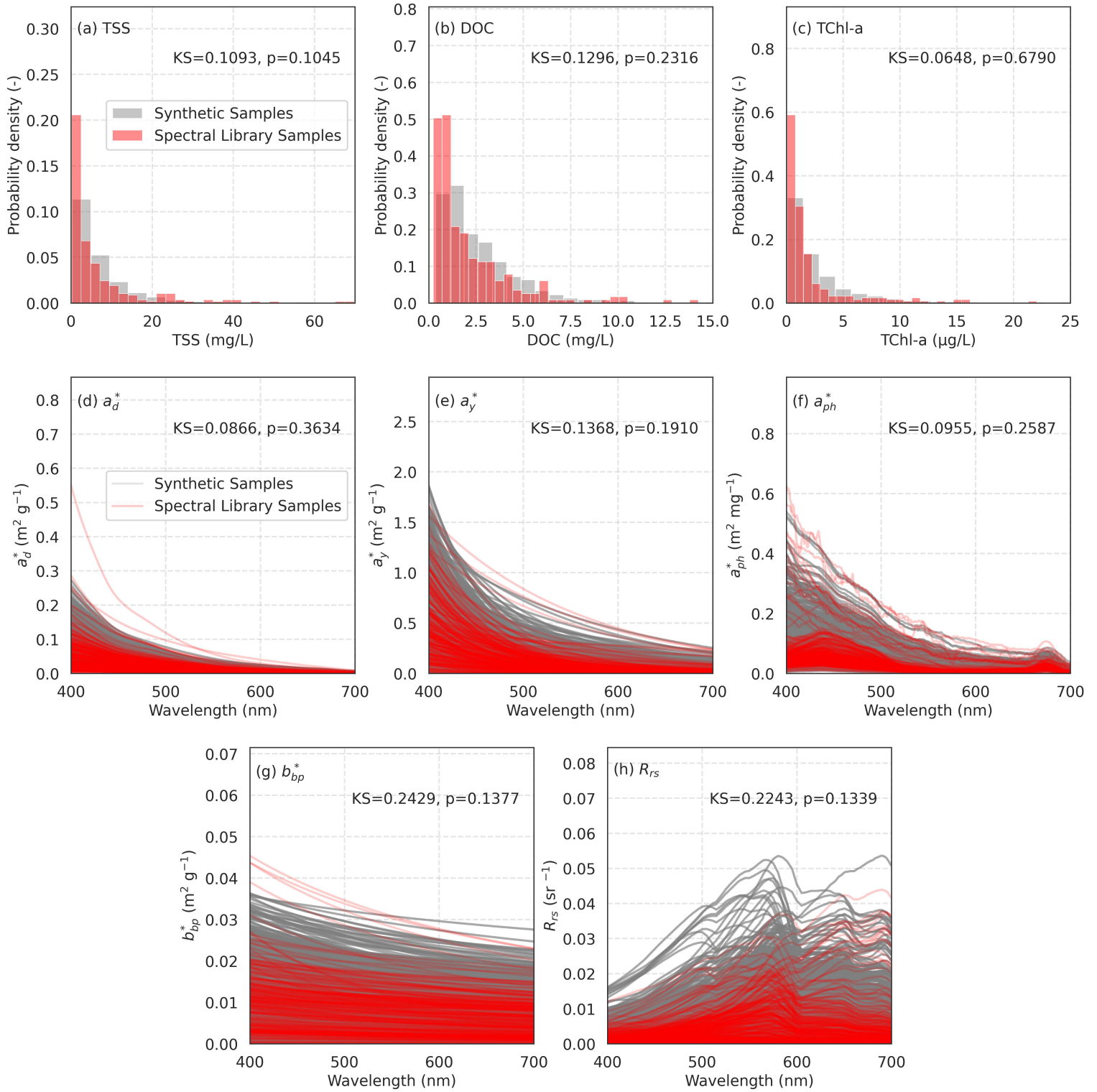


Figure 7: Comparisons between samples from the synthetic dataset \mathcal{D} with those from the in situ spectral library for (a–c) biogeochemical parameters (TSS, DOC, and TChl-a), (d–g) specific inherent optical properties (a_d^* , a_y^* , a_{ph}^* , and b_{bp}^*), and (h) the corresponding remote sensing reflectance R_{rs} . Results of the Kolmogorov–Smirnov (KS) test, including test statistics and p-values, are reported within each subplot. Please refer to the nomenclature in Table 1 for definitions of symbols and acronyms.

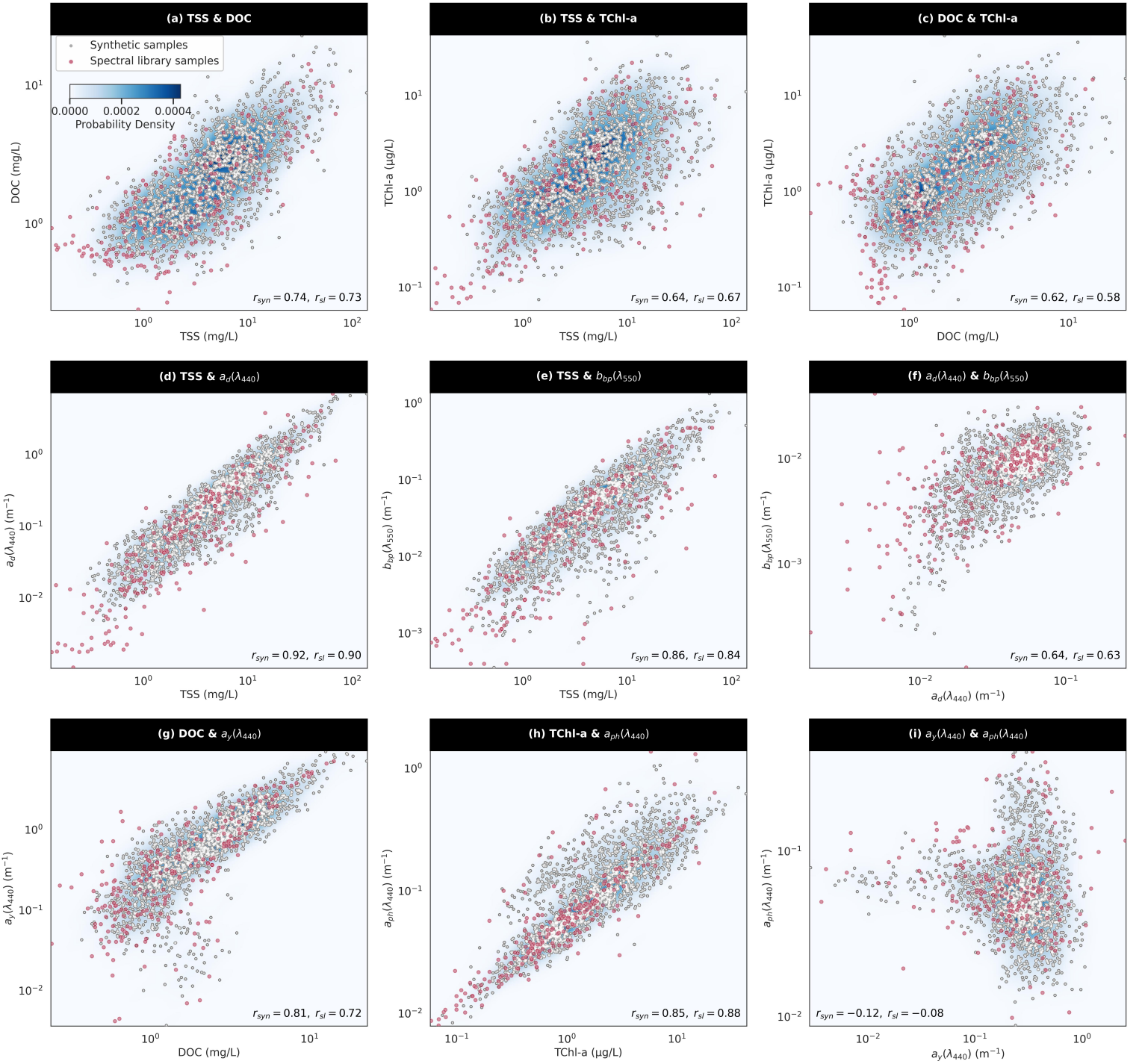


Figure 8: Comparison of parameter correlations between synthetic samples and spectral library samples for the joint distributions of (a) TSS and DOC, (b) TSS and TChl-a, (c) DOC and TChl-a, (d) TSS and $a_d(\lambda_{440})$, (e) TSS and $b_{bp}(\lambda_{550})$, (f) $a_d(\lambda_{440})$ and $b_{bp}(\lambda_{550})$, (g) DOC and $a_y(\lambda_{440})$, (h) TChl-a and $a_{ph}(\lambda_{440})$, and (i) $a_y(\lambda_{440})$ and $a_{ph}(\lambda_{440})$. Background colour indicates the probability density of the joint distributions. r_{syn} and r_{sl} stand for the Pearson correlation coefficients between synthetic samples and spectral library samples, respectively. Please refer to the nomenclature in Table 1 for definitions of other symbols and acronyms.

the spectral library scatters. Therefore, synthetic samples drawn from the DP-GMM probability estimates align well with the spectral library samples, not only matching the overall range of values but also preserving the underlying correlations between parameters.

4.4. Accuracies of BGC parameter retrieval

Fig. 9 shows the relationship between predicted and measured concentrations of TSS, DOC, and TChl-a across the five experimental sites of Fitzroy Estuary, Keppel Bay, Boston Bay, Cockburn Sound, and Lucinda Jetty. The accuracies shown in the figure were assessed with r^2 , bias, RMSE, and MAE between the predicted and measured values. Across all sites, TSS showed an r^2 of 0.916 with a bias of 1.10, RMSE of 1.67, and MAE of 1.45. For DOC, r^2 was 0.539, with a bias of 1.05, RMSE of 1.52, and MAE of 1.36. TChl-a showed an r^2 of 0.683, with a bias of 1.08, RMSE of 1.60, and MAE of 1.41.

While Fig. 9 presents the overall accuracy assessment aggregated across all experimental sites, we further disaggregated the evaluation by site to examine the regional retrieval performance of the proposed approach. Fig. 10 summarises the site-specific results, showing RMSE and MAE for TSS, DOC, and TChl-a at each individual experimental site. For TSS retrieval, RMSE values range from 1.54 for the Boston Bay/Cockburn Sound sites to 1.76 for the Lucinda Jetty site, with corresponding MAE values from 1.46 to 1.51. The relatively low TSS retrieval errors observed in Boston Bay and Cockburn Sound may be attributed to the low riverine influence at these experimental sites which contributes to the low inherent variability evident in these datasets (Fig. 9a) (Table 2). In contrast, Fitzroy Estuary, Keppel Bay, and Lucinda Jetty are subject to moderate to high river discharge (Table 2), which can introduce sediment loads and increase the variability of suspended sediments. Such enhanced sediment dynamics likely complicate the TSS- R_{rs} relationship, contributing to the comparatively higher retrieval errors at these river-influenced sites. For DOC, retrieval errors are comparatively consistent across regions, with RMSE values between 1.24 for the Lucinda Jetty site and 1.69 for the Keppel Bay site, and the corresponding MAE between 1.22 and 1.60. For TChl-a retrieval, the RMSE values ranging from 1.32 for the Fitzroy Estuary site to 1.85 for the Lucinda Jetty site, and the corresponding MAE values from 1.30 to 1.61. The largest error in TChl-a retrieval was observed at Lucinda Jetty, which could be attributed to its subtropical location and adjacency to the Great Barrier Reef, as this region is characterised by diverse phytoplankton communities and dynamic biological activities. When averaged across all sites, the retrieval performance results in RMSE values of 1.64 for TSS, 1.40 for DOC, and 1.59 for TChl-a, with corresponding MAE values of 1.51, 1.36, and 1.47, respectively.

Table 6 compares the predictive accuracy of the proposed method against five benchmark models, including three empirical models (Choo et al., 2022; Cherukuru et al., 2016b, 2019) and two deep learning models (DL-RS (Unnithan et al., 2025) and HyperEST (Luo et al., 2025)). It was observed from the table that the proposed

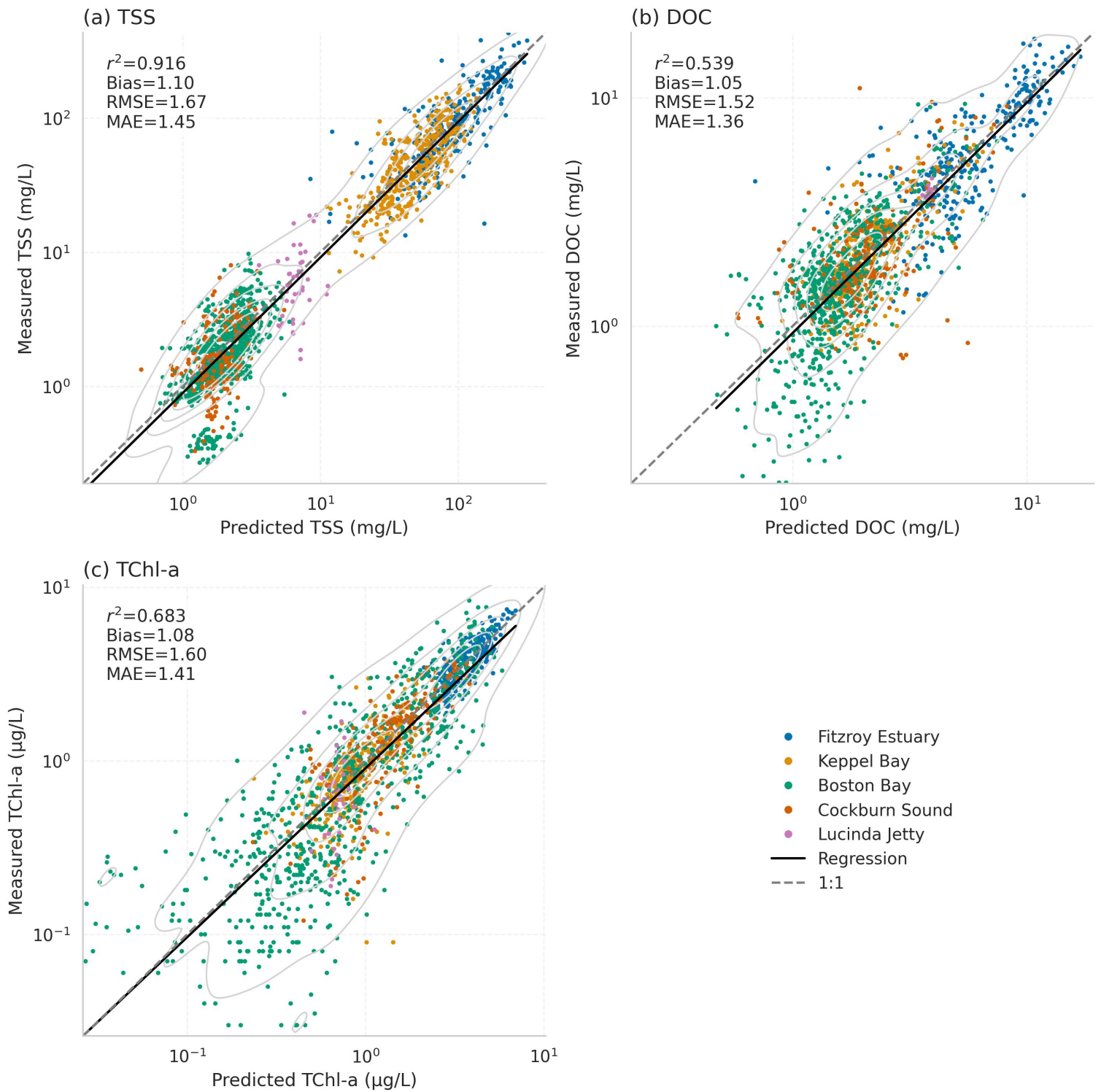


Figure 9: Comparison between predicted and measured concentrations of (a) total suspended solids (TSS), (b) dissolved organic carbon (DOC), and (c) total chlorophyll-a (TChl-a) across the five experimental sites of Fitzroy Estuary, Keppel Bay, Boston Bay, Cockburn Sound, and Lucinda Jetty. Axes are shown on \log_{10} scales. Accuracies were assessed using the coefficient of determination (r^2), bias, root mean square error (RMSE), and mean absolute error (MAE) as defined in Eq. (22). Grey lines represent contours of equal probability mass for the purpose of enhancing visualisation of the data distribution.

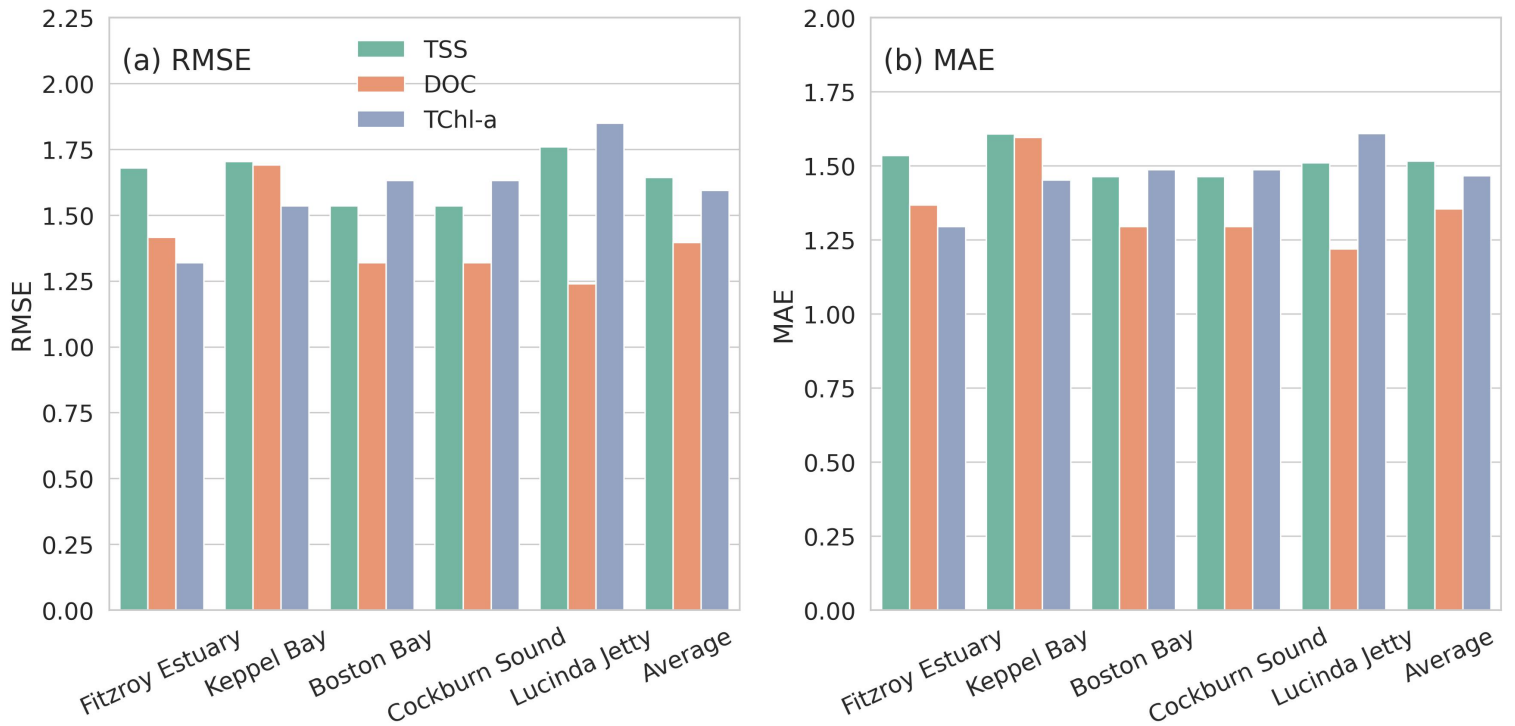


Figure 10: (a) Root mean squared error (RMSE) and (b) mean absolute error (MAE) of total suspended solids (TSS), dissolved organic carbon (DOC), and total chlorophyll-a (TChl-a) concentrations retrieved using the proposed approach, evaluated for each individual experimental site of Fitzroy Estuary, Keppel Bay, Boston Bay, Cockburn Sound, and Lucinda Jetty, as well as for the overall performance averaged across all sites.

approach generally outperforms the benchmark models in terms of r^2 , RMSE, and MAE in the retrieval accuracies of TSS, DOC, and TChl-a. For TSS, it achieves the highest accuracy with the best r^2 (0.92), RMSE (1.67), and MAE (1.45), while remaining competitive in bias compared to HyperEST and DL-RS. For DOC, the proposed method improves performance over both the empirical model and DL-RS, increasing r^2 from 0.17 to 0.54 and reducing RMSE and MAE by a notable margin, although its bias is slightly higher than DL-RS. For TChl-a, the proposed model shows promising results across the metrics, outperforming both the empirical model and HyperEST, with a gain in r^2 (0.68) and error reduction in bias, RMSE, and MAE. Given the structural differences among these models (Table 4), the improved accuracy could be attributed to the physics-aware pretraining and regional adaptation adopted by the proposed approach.

4.5. Time-series analysis of BGC and R_{rs} data

Fig. 11 shows time-series variations in hyperspectral R_{rs} and corresponding BGC parameters (TSS, DOC, and TChl-a) and ancillary physical variables (temperature and salinity) at the experimental site of Fitzroy Estuary, with Fig. 11a showing data over the entire experimental period from 26 April 2023 to 10 July 2024, and Fig. 11b showing the zoomed-in view for the period between 10 March and 31 May 2024. It was observed

Table 6: Comparison of retrieval accuracies between the proposed approach and benchmark models for total suspended solids (TSS), dissolved organic carbon (DOC), and total chlorophyll-a (TChl-a). Benchmark methods include empirical models for TSS (Choo et al., 2022), DOC (Cherukuru et al., 2016b), and TChl-a (Cherukuru et al., 2019), as well as the deep learning models DL-RS (Unnithan et al., 2025), which is applied to TSS and DOC retrieval, and HyperEST (Luo et al., 2025), which is applied to TSS and TChl-a retrieval. Performance is evaluated using the coefficient of determination (R^2), bias, root mean square error (RMSE), and mean absolute error (MAE), as defined in Eq. (22). The best and second-best results are shown in bold and underlined, respectively.

Variable	Model	r^2	Bias	RMSE	MAE
TSS	Choo et al. (2022)	0.58	1.54	3.34	2.42
	DL-RS (Unnithan et al., 2025)	0.89	<u>1.03</u>	1.77	<u>1.52</u>
	HyperEST (Luo et al., 2025)	<u>0.91</u>	1.02	<u>1.76</u>	1.55
	Proposed	0.92	1.10	1.67	1.45
DOC	Cherukuru et al. (2016b)	0.12	1.28	2.26	1.85
	DL-RS (Unnithan et al., 2025)	<u>0.17</u>	0.93	<u>1.94</u>	<u>1.70</u>
	Proposed	0.54	<u>1.05</u>	1.52	1.36
TChl-a	Cherukuru et al. (2019)	0.09	1.64	3.25	2.53
	HyperEST (Luo et al., 2025)	<u>0.59</u>	<u>1.14</u>	<u>2.12</u>	<u>1.70</u>
	Proposed	0.68	1.08	1.60	1.41

from the figure that, the Fitzroy Estuary site, characterised by high river influence and a subtropical climate (Table 2), exhibits high TSS concentrations with a periodic variability over time, alongside elevated and highly dynamic levels of DOC and TChl-a. The periodic variability likely reflects the combined influence of tidal cycles and fluctuations in Fitzroy River discharge, as evidenced by the salinity variations shown in the figure, which indicate varying degrees of mixing between river water and seawater.

The time series of R_{rs} at the Fitzroy Estuary site (Fig. 11) shows relatively high R_{rs} values, reaching up to approximately 0.08 sr^{-1} , particularly in the green to red spectral region (550–650 nm). The time-series R_{rs} measurements also exhibit pronounced temporal variability, including a periodic pattern over the observation period (Fig. 11). Given that the Fitzroy Estuary is a river-influenced system characterised by relatively high TSS concentrations, the elevated R_{rs} in the green-to-red region is likely driven by enhanced particulate backscattering associated with high sediment loads. The observed periodic variability in R_{rs} may further reflect temporal

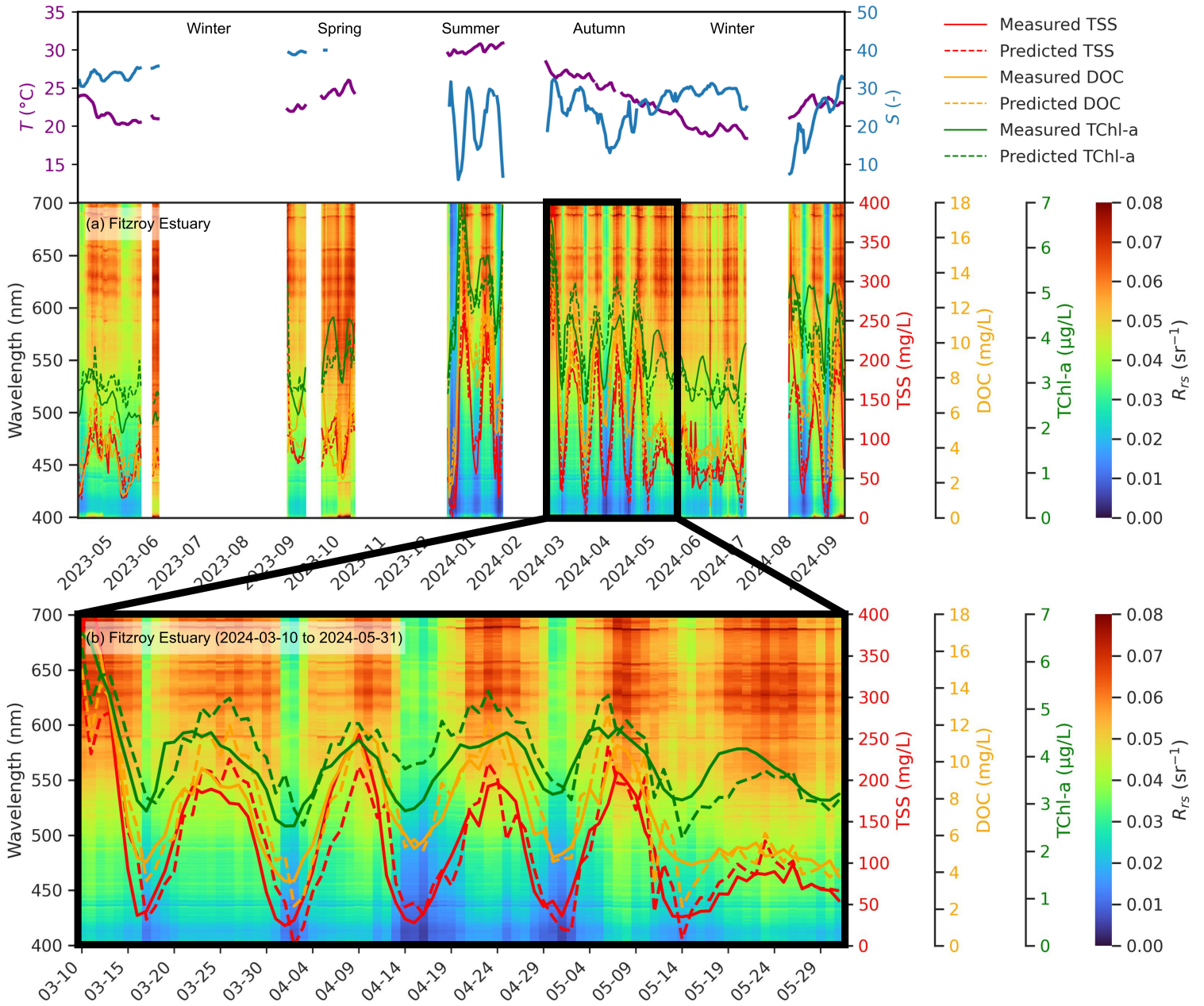


Figure 11: (a) Temporal variation of water-leaving remote sensing reflectance (R_{rs}) and corresponding in situ measurements of temperature (T), salinity (S), total suspended solids (TSS), dissolved organic carbon (DOC), and total chlorophyll-a (TChl-a) at the experimental site of Fitzroy Estuary over the experimental period from 26 April 2023 to 23 September 2024. The BGC values predicted from hyperspectral R_{rs} observations using the proposed approach are also shown in the figure. (b) Zoomed-in view for the period between 10 March and 31 May 2024, showing both measured and model-predicted concentrations of the BGC parameters. Background colour shows hyperspectral R_{rs} as a function of wavelength (400–700 nm) and time. Blank regions in the plots denote periods of instrument malfunction.

changes in BGC properties, influenced by tidal dynamics and variations in river discharge.

Fig. 12 shows time-series variations in R_{rs} , TSS, DOC, TChl-a, temperature, and salinity at the Keppel Bay site over the experimental period from 1 June 2023 to 28 November 2024. This site is located downstream of the Fitzroy Estuary site and is closer to the open ocean. Accordingly, higher salinity was observed at Keppel Bay compared with the Fitzroy Estuary site. For the BGC parameters, concentrations of TSS, DOC, and TChl-a at the Keppel Bay site are generally lower than those at the Fitzroy Estuary site. Periodic variations are also evident in the time-series BGC measurements at the Keppel Bay site, although they are less pronounced than those observed at the Fitzroy Estuary site. As compared with the Fitzroy Estuary site, lower levels of R_{rs} were observed at the Keppel Bay site, as shown in Fig. 12. The peak R_{rs} is generally below 0.04 sr^{-1} and centred in the green spectral region around 550 nm.

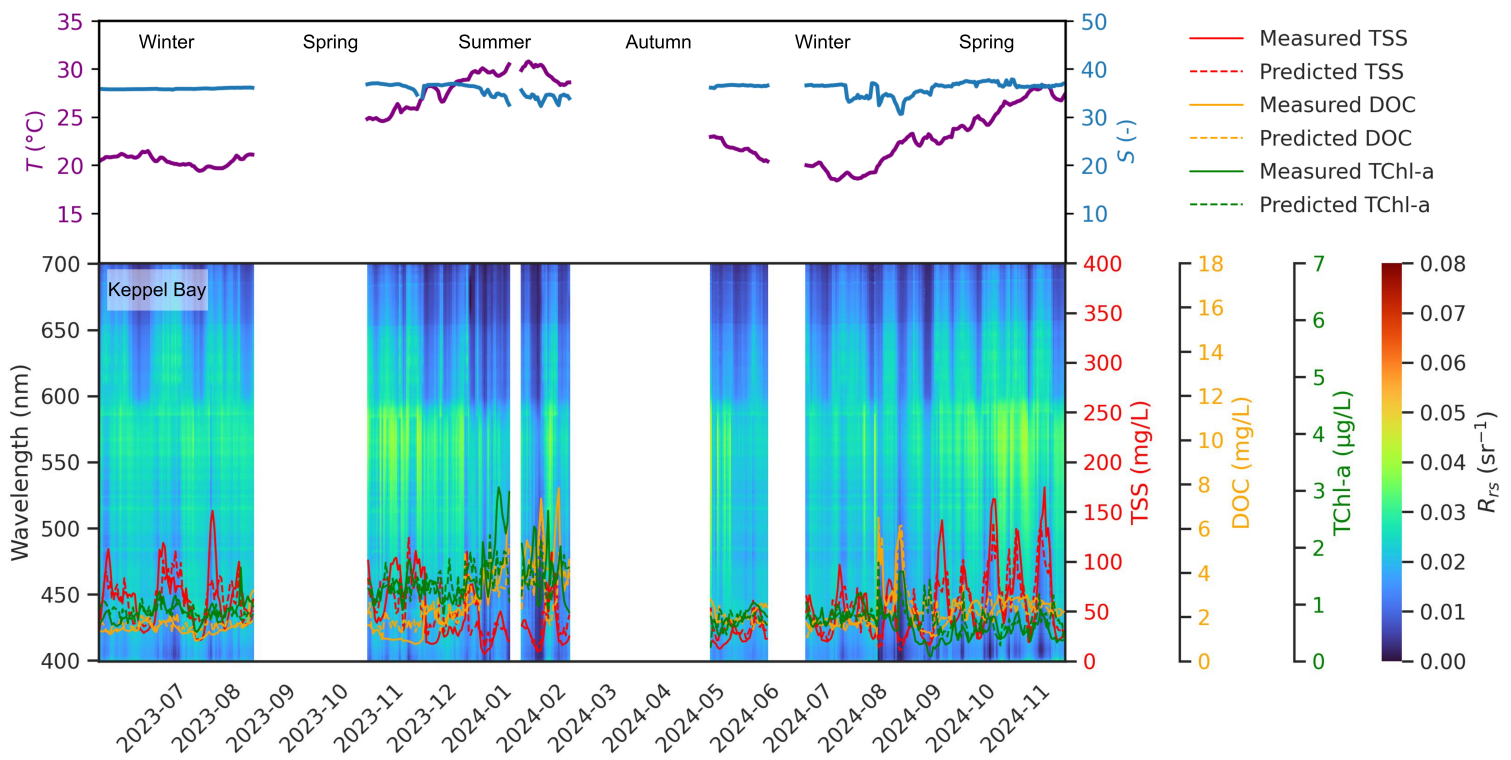


Figure 12: Temporal variation of water-leaving remote sensing reflectance (R_{rs}) and corresponding in situ measurements of temperature (T), salinity (S), total suspended solids (TSS), dissolved organic carbon (DOC), and total chlorophyll-a (TChl-a) at the experimental site of Keppel Bay over the experimental period from 1 June 2023 to 28 November 2024. The BGC values predicted from hyperspectral R_{rs} observations using the proposed approach are also shown in the figure. Background colour shows hyperspectral R_{rs} as a function of wavelength (400–700 nm) and time. Blank regions in the plots denote periods of instrument malfunction.

Fig. 13 shows time-series variations in R_{rs} , TSS, DOC, TChl-a, temperature, and salinity at the Boston Bay site over the experimental period from 1 September 2022 to 2 February 2025. Different from the subtropical

Fitzroy Estuary and Keppel Bay sites, the Boston Bay site is a temperate site without direct river influence (Table 2). Accordingly, it was observed from Fig. 13 that the the Boston Bay site is characterised by consistently low TSS and DOC and minimal temporal variability, indicative of clearer and more optically stable waters. The R_{rs} levels at the Boston Bay site are generally lower than the Fitzroy Estuary and Keppel Bay sites, with the peak R_{rs} below 0.015 sr^{-1} and centred in the green/blue spectral region of 450–550 nm.

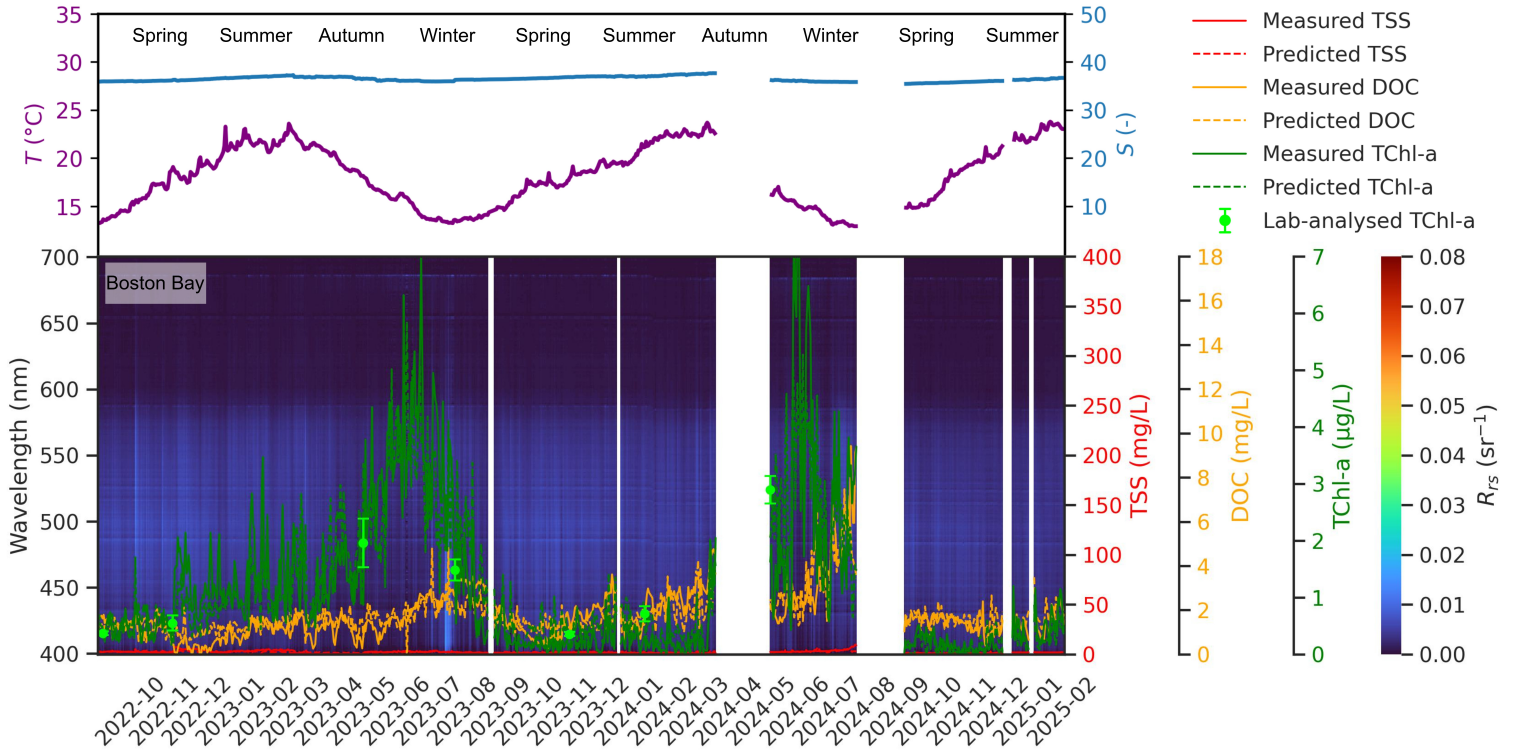


Figure 13: Temporal variation of water-leaving remote sensing reflectance (R_{rs}) and corresponding in situ measurements of temperature (T), salinity (S), total suspended solids (TSS), dissolved organic carbon (DOC), and total chlorophyll-a (TChl-a) at the experimental site of Boston Bay over the experimental period from 1 September 2022 to 2 February 2025. Background colour shows hyperspectral R_{rs} as a function of wavelength (400–700 nm) and time. The BGC values predicted from hyperspectral R_{rs} observations using the proposed approach are also shown in the figure. Laboratory-analysed grab samples of TChl-a (mean \pm standard deviation) are shown as light green markers with error bars. Blank regions in the plots denote periods of instrument malfunction.

An important observation from Fig. 13 is the clear seasonal pattern in TChl-a concentrations at the Boston Bay site, which increase during the winter months. This seasonal rise begins around March/April each year over the experimental period, remains elevated throughout winter, and declines to lower levels by July/August. To verify this pattern, grab samples were collected at the Boston Bay site on several occasions during the experiment, and TChl-a concentrations were analysed by the CSIRO Hydrochemistry Laboratories in Hobart,

Tasmania. As shown in Fig. 13, the laboratory-analysed TChl-a values are in good agreement with the in situ time-series measurements, consistently showing higher concentrations between March/April and July/August. In 2025, the year following the experimental period of this study, a harmful algal bloom broke out in March along the South Australian coast⁴, including the Boston Bay region, resulting in mass fish deaths and significant impacts on marine ecosystems, fisheries, aquaculture, tourism, and coastal activities. The observation reported in this study may therefore provide important baseline information on seasonal phytoplankton dynamics and could contribute to a better understanding of environmental conditions that precede or favour the development of such bloom events.

Fig. 14 shows time-series variations in R_{rs} , TSS, DOC, TChl-a, temperature, and salinity at the Cockburn Sound site over the experimental period from 15 July 2023 to 18 February 2024. As observed from the figure, Cockburn Sound, being a temperate embayment with low riverine influence (Table 2), exhibits generally low to moderate concentrations of TSS, DOC, and TChl-a over the experimental period, with some temporal variability. Correspondingly, this site displays relatively low R_{rs} values, with peak R_{rs} typically below 0.02 sr^{-1} and centred in the green spectral region around 500–550 nm.

It was also observed from Figs. 11–14 that, despite clear regional differences among the experimental sites, the BGC parameters predicted from hyperspectral R_{rs} observations using the proposed method generally agree well with the in situ BGC measurements in both magnitude and temporal dynamics. This consistency demonstrates the capability of in situ hyperspectral sensing to reliably capture BGC variability over time, showing its potential as a cost-effective approach for continuous time-series monitoring of water quality.

4.6. Analysis of regional distinctions

Fig. 15 shows the regional distinctions among the experimental sites in their BGC and R_{rs} distributions. Fig. 15a shows the distribution of TSS, DOC, and TChl-a concentrations in the BGC feature space across the five experimental sites. Fitzroy Estuary exhibits the highest TSS and DOC concentrations overall, with moderate to elevated TChl-a levels. Keppel Bay is characterised by moderate TSS and DOC concentrations but comparatively lower TChl-a values. Boston Bay and Cockburn Sound cluster towards lower TSS and DOC concentrations, with Boston Bay showing a broader spread in TChl-a than Cockburn Sound. Lucinda Jetty shows moderate TSS, DOC, and TChl-a values as compared with other sites.

In the CIE 1931 chromaticity diagram shown in Fig. 15b, the R_{rs} measurements display distinct colour groupings that reflect differences in apparent water colour among the regions. Waters from Fitzroy Estuary display brown colours, characteristic of turbid estuarine conditions. Keppel Bay exhibits less brown colours due

⁴https://en.wikipedia.org/wiki/2025_algal_bloom_in_South_Australia

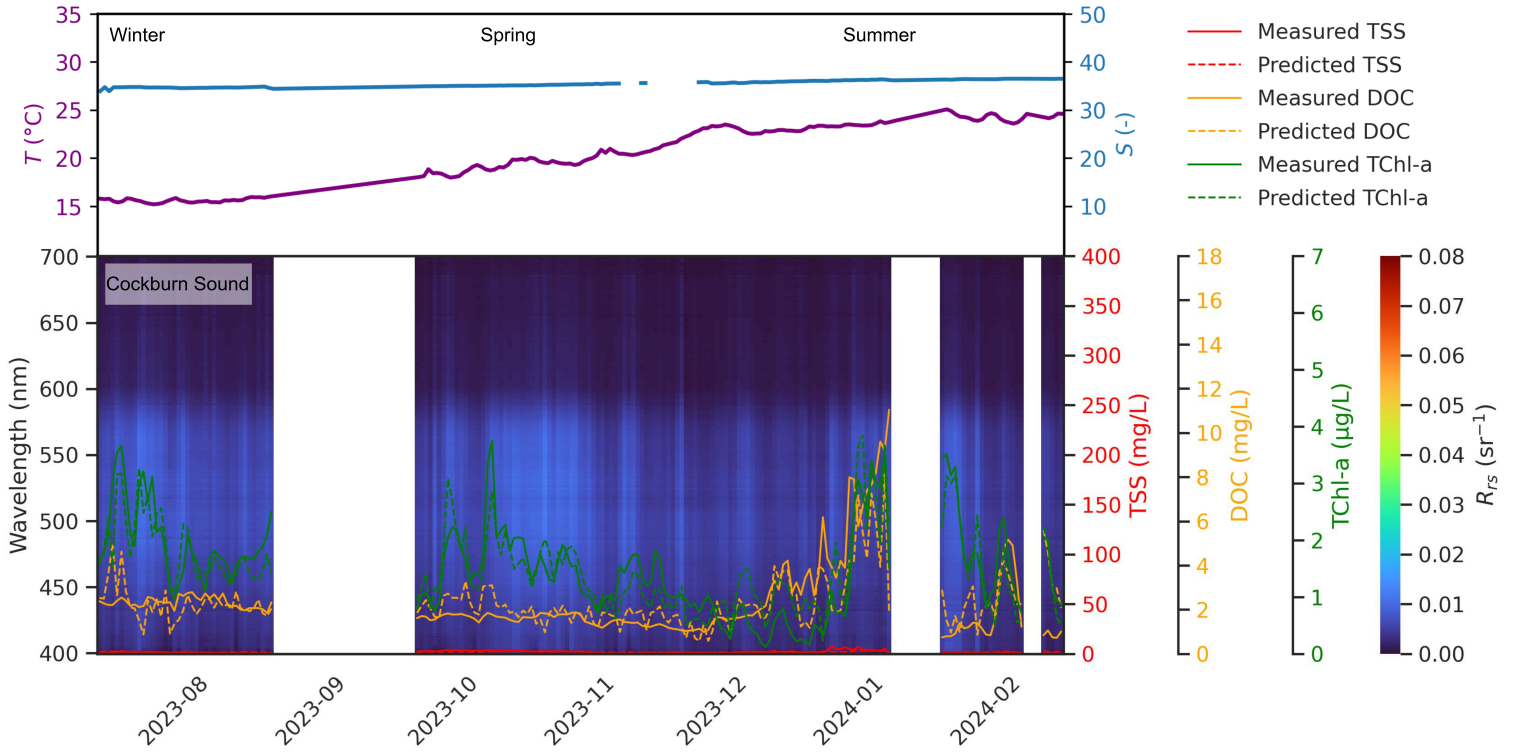


Figure 14: Temporal variation of water-leaving remote sensing reflectance (R_{rs}) and corresponding in situ measurements of temperature (T), salinity (S), total suspended solids (TSS), dissolved organic carbon (DOC), and total chlorophyll-a (TChl-a) at the experimental site of Cockburn Sound over the experimental period from 15 July 2023 to 18 February 2024. The BGC values predicted from hyperspectral R_{rs} observations using the proposed approach are also shown in the figure. Background colour shows hyperspectral R_{rs} as a function of wavelength (400–700 nm) and time. Blank regions in the plots denote periods of instrument malfunction.

to moderate river influence. Boston Bay and Cockburn Sound are associated with clearer green to blue-green waters, typical of less turbid coastal environments with lower suspended sediment loads. Lucinda Jetty is more green-coloured than the clearer coastal sites but less brown than the estuarine waters.

In summary, the regional distinctions observed in Fig. 15 are clearly reflected in both the BGC parameters and their corresponding optical responses across the experimental sites. This variability suggests that constituent dynamics and R_{rs} characteristics are region-dependent. These findings highlight the need to develop region-adaptable approaches for BGC parameter retrieval to ensure robust, accurate, and transferable performance across diverse coastal and estuarine water environments.

4.7. Comparison with existing methods

Traditional empirical methods for BGC retrieval from hyperspectral data rely on simple statistical relationships between R_{rs} and target variables. The BGC parameters are typically estimated using wavelength-specific

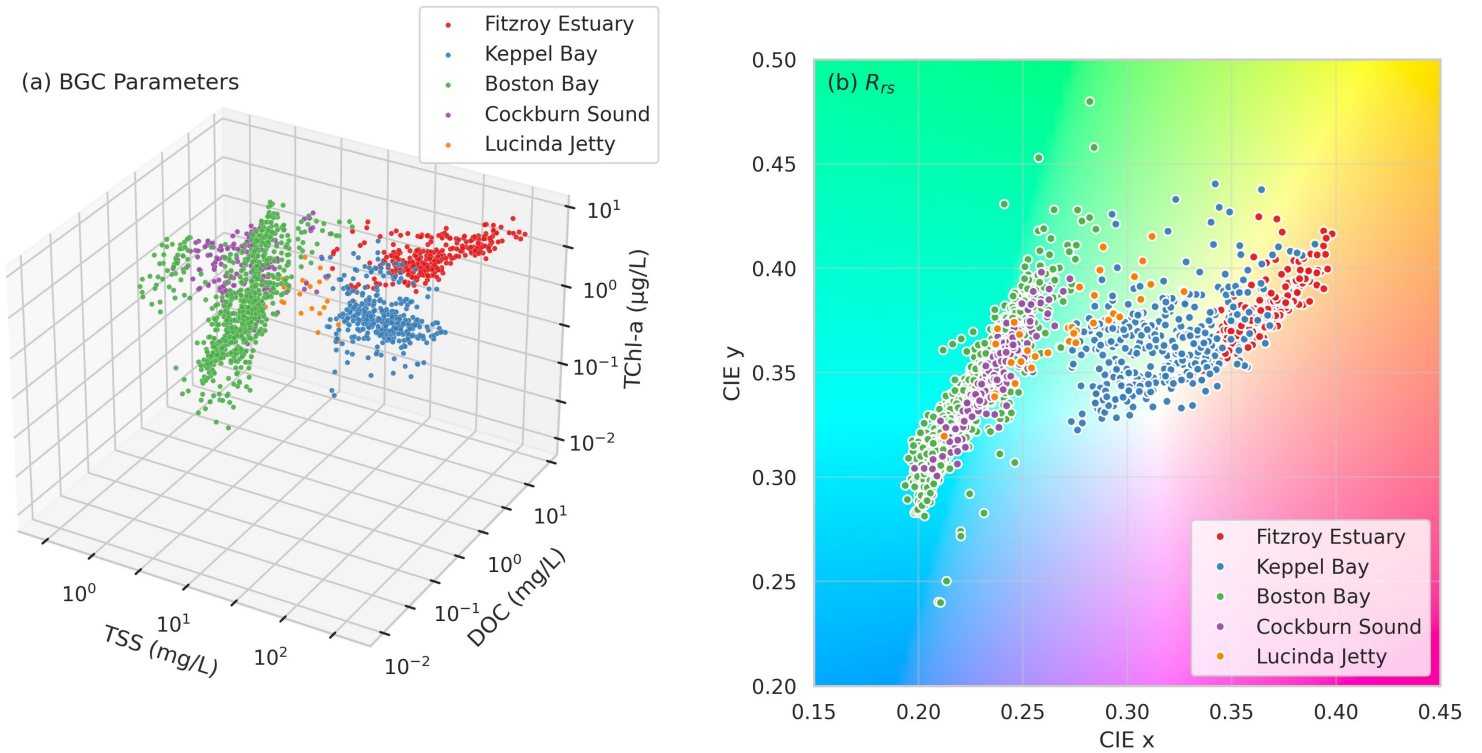


Figure 15: (a) Distribution of biogeochemical (BGC) parameters, including total suspended solids (TSS), dissolved organic carbon (DOC), and total chlorophyll-a (TChl-a) concentrations, at the experimental sites of Fitzroy Estuary, Keppel Bay, Boston Bay, Cockburn Sound, and Lucinda Jetty. (b) The International Commission on Illumination (CIE) 1931 chromaticity diagram showing the distribution of water-leaving remote sensing reflectance (R_{rs}) measured at these experimental sites.

R_{rs} ratios, such as the green/red ratio for TSS (Choo et al., 2022), the blue/green ratio for TChl-a (Cherukuru et al., 2019), and the ratio between two blue bands linked to CDOM absorption for DOC (Cherukuru et al., 2016b), with coefficients fitted to local observations. While these approaches are computationally efficient and easy to interpret, their applicability is typically limited to the specific regions and conditions under which they were developed, because the underlying relationships between R_{rs} and BGC parameters are highly non-linear and strongly influenced by local bio-optical properties. As a result, empirical models often require frequent recalibration and tend to perform poorly when transferred to optically complex waters where the BGC- R_{rs} relationship becomes highly non-linear, variable, and influenced by multiple interacting bio-optical constituents.

To overcome these limitations and better capture the underlying intricate and regionally variable relationships, data-driven modelling has increasingly been adopted for hyperspectral retrieval of aquatic BGC constituents. Recent studies on data-driven approaches have progressed along three main directions: (1) multi-distribution probabilistic modelling with aggregated large datasets (*e.g.*, O'Shea et al. (2023)), (2) deep learning models leveraging augmented synthetic datasets (*e.g.*, Unnithan et al. (2025)), and (3) self-supervised approaches

that learn representations from unlabelled spectra (*e.g.*, Luo et al. (2025)). O’Shea et al. (2023) developed a global hyperspectral inversion framework based on mixture density networks (MDNs), which simultaneously retrieves multiple BGC parameters IOPs while addressing the non-unique inversion problem through probabilistic modelling. Although this approach achieves strong global generalisation, it relies on extensive labelled datasets and does not explicitly account for regional bio-optical variability. In contrast, the present study adopts a two-stage strategy that incorporates physical knowledge prior to regional calibration, thereby explicitly accommodating regional distinctions in the modelling process. Unnithan et al. (2025) utilised forward-model-based synthetic data for training a deep learning model called DL-RS, but primarily as a means of augmenting training datasets for supervised inversion at regional scales. In DL-RS, synthetic and observed data are combined directly to improve performance, whereas in our framework synthetic data play a distinct role in physics-aware pretraining, enabling a base model to first learn generalised BGC–IOP– R_{rs} relationships from large-scale simulations before being adapted to specific regions using sparse observations. This separation between pretraining and adaptation allows the model to learn physics-aware transferable representations rather than fitting directly to a particular dataset, and thus supports efficient adaptation to optically diverse environments where in situ data are limited. Luo et al. (2025) identified the limited transferability of conventional supervised models to unseen complex waters and proposed HyperEst, a self-supervised framework that learns spectral representations from large volumes of unlabelled R_{rs} data using a context-aware autoencoder, improving data efficiency and cross-sensor generalisation. However, the self-supervised pretraining stage in HyperEst is data-driven and does not explicitly incorporate bio-optical knowledge. By comparison, the present study integrates prior physical knowledge derived from bio-optical forward modelling, constrained by measured BGC parameters and IOPs/SIOPs from a representative spectral library. Therefore, while HyperEst enhances robustness through self-supervised learning, our approach improves adaptability through explicit physical regularisation and targeted region-specific fine-tuning.

Overall, the proposed approach distinguishes itself from existing approaches by integrating physical principles into a deep learning framework, enabling physically consistent and region-adaptive modelling of the BGC– R_{rs} relationship while reducing the reliance on region-specific in situ training samples. This integrated framework provides a flexible and transformable solution for hyperspectral retrieval of BGC parameters across diverse bio-optical environments.

4.8. Limitations and prospects

Timely, accurate, and continuous monitoring of water quality is essential for effective management of aquatic ecosystems, especially for Australian coastal waters that are increasingly subject to anthropogenic and climate-driven pressures. Hyperspectral remote sensing has demonstrated strong potential for cost-effective retrieval

of optically active BGC parameters. However, the transferability of retrieval algorithms across different water bodies remains limited, as the relationship between spectral observations and BGC parameters varies substantially among regions due to differences in inherent bio-optical characteristics. To address this challenge, we developed in this study a framework that first trains a region-agnostic base model using synthetic data generated by a physics-based bio-optical model. The base model is subsequently adapted to individual sites through fine-tuning with a small number of in-situ samples. We evaluated the proposed approach across five coastal sites in Australia, each characterised by distinct bio-optical properties. While the experimental results demonstrated the effectiveness of the proposed approach, several limitations remain, as discussed in the following, offering opportunities for future improvement.

Firstly, the current evaluation is limited to five sites in Australian coastal waters. While these sites span distinct coastal and estuarine regimes, they do not fully represent the broader range of optical water types observed across global coastal environments. Expanding the evaluation to include a more diverse set of coastal optical regimes would improve the robustness of the assessment and help better characterise the model’s ability to generalise across varying bio-optical conditions

Secondly, this study uses near-surface hyperspectral R_{rs} as the primary observation source. Future work could focus on extending the framework to spaceborne multi/hyperspectral imagery, which offers the potential for regional-to-global monitoring at consistent revisit intervals (*e.g.*, Yang et al. (2025); Guo et al. (2019); Zhao et al. (2024)). However, moving from in situ to satellite retrieval introduces additional error sources (*e.g.*, atmospheric correction uncertainty, adjacency effects in narrow/complex water bodies, and sensor-specific spectral response), which can degrade retrieval performance if not explicitly accommodated. Recent and ongoing imaging spectroscopy missions, such as PRISMA (Pignatti et al., 2013), DESIS (Krutz et al., 2019; Guo et al., 2022, 2023), and EnMAP (Chabrillat et al., 2024), provide an increasingly practical pathway for spaceborne hyperspectral water quality applications, motivating dedicated adaptation and benchmarking of the proposed approach under satellite observation conditions.

Finally, the current study focuses on three optically active BGC parameters, namely TSS, DOC, and TChl-a, where hyperspectral R_{rs} spectra provide information through absorption and backscattering features. Some other water quality parameters, such as nitrate and nitrite, are also important indicators of nutrient enrichment and eutrophication risk in aquatic ecosystems (Pan et al., 2018). Future work could be carried out to extend the proposed framework to these parameters. However, this extension is challenging, as nitrate and nitrite are optically inactive in the visible spectral region (Pan et al., 2018; Guo et al., 2025b). Therefore, their correlations with optically active constituents (*e.g.*, TSS, DOC, and TChl-a) and the incorporation of ancillary predictors (*e.g.*, temperature and salinity) would likely need to be leveraged in the modelling.

5. Conclusion

This study presented a region-adaptable framework for retrieving key BGC parameters, including TSS, DOC, and TChl-a, from in situ hyperspectral R_{rs} measurements. The proposed method integrates physical knowledge with a data-driven learning strategy through a two-stage physics-aware meta-learning framework. In the first stage, a physics-based bio-optical forward model was used to generate a large synthetic dataset from a continental bio-optical spectral library. This dataset was then used to pretrain a region-agnostic base model with meta-learning, allowing the model to learn fundamental physical relationships. In the second stage, the pretrained base model was adapted to individual regions using local in situ observations, allowing the framework to account for region-specific bio-optical variability.

The proposed approach was evaluated using hyperspectral R_{rs} and BGC observations collected from five geographically distinct coastal sites across Australia, representing a wide range of environmental and bio-optical conditions. The retrieval accuracies showed good agreement between predicted and measured values, demonstrating that the model successfully captured the relationships between hyperspectral R_{rs} and BGC parameters across bio-optically distinct regions. Comparison experiments showed that the proposed approach outperformed five existing methods commonly used for TSS, DOC, and TChl-a retrieval, which could be attributed to the adoption of physics-aware pretraining and region-specific adaptation in the proposed approach. These results indicate that the proposed framework provides reliable and accurate retrieval of BGC parameters across different coastal environments. Time-series analyses across the experimental sites demonstrated that the predicted BGC parameters closely matched the temporal variability observed in the in situ measurements. This highlights the potential of in situ hyperspectral sensing as a cost-effective approach for continuous monitoring of coastal water quality, particularly in regions where traditional sampling campaigns are logistically challenging or resource intensive.

While the results are promising, there remain opportunities for further improvement. The current evaluation focuses on a limited number of coastal and estuarine sites, which may not fully represent the broader diversity of optical water types, particularly inland waters with stronger spatiotemporal variability. Future work should extend validation to additional aquatic environments and explore the application of the proposed framework to satellite-based hyperspectral observations. Such developments would enable regional-to-global monitoring of water quality and further enhance the operational applicability of physics-aware data-driven approaches for aquatic ecosystem monitoring.

CRedit authorship contribution statement

Yiqing Guo: Methodology, Software, Formal Analysis, Data Curation, Writing - Original Draft. **Nagur R. C. Cherukuru:** Conceptualisation, Formal Analysis, Data Curation, Writing - Review & Editing, Project Administration, Funding Acquisition. **Eric A. Lehmann:** Conceptualisation, Writing - Review & Editing, Project Administration, Funding Acquisition. **S. L. Kesav Unnithan:** Software, Data Curation, Writing - Review & Editing. **Tim J. Malthus:** Data Curation, Writing - Review & Editing. **Gemma Kerrisk:** Data Curation, Writing - Review & Editing. **Xiubin Qi:** Data Curation, Writing - Review & Editing. **Faisal Islam:** Data Curation, Writing - Review & Editing. **Tisham Dhar:** Data Curation, Writing - Review & Editing. **Mark J. Doubell:** Funding Acquisition, Data Curation, Writing - Review & Editing.

Declaration of competing interest

The authors declare that they have no known competing financial interests or personal relationships that could have appeared to influence the work reported in this paper.

Acknowledgements

The authors would like to sincerely thank the following organisations and services for their support to this work: Commonwealth Scientific and Industrial Research Organisation (CSIRO) AquaWatch Australia Mission, CSIRO AI4Missions, South Australian Research and Development Institute (SARDI), CSIRO Data61, CSIRO Environment, CSIRO Space and Astronomy, CSIRO Earth Analytics Science and Innovation (EASI) platform, and CSIRO AquaWatch Data Service (ADS).

The authors would like to acknowledge the in situ data from Lucinda Jetty Coastal Observatory (Principal Investigator: Dr Thomas Schroeder with CSIRO Environment). These data were sourced from Australia's Integrated Marine Observing System (IMOS). IMOS is enabled by the National Collaborative Research Infrastructure Strategy (NCRIS). It is operated by a consortium of institutions as an unincorporated joint venture, with the University of Tasmania as Lead Agent.

We acknowledge the SARDI field team (Mr Ian Moody and Mr Paul Malthouse) for their help with Boston Bay buoy setup and maintenance. Thanks also go to CSIRO's EASI team for their guidance on the ADS platform, and Ms Florina Richard with CSIRO Environment and Dr Foivos Diakogiannis with CSIRO Data61 for helpful discussions. We are grateful to Dr Albertina Dias with CSIRO Hydrochemistry Laboratories, Hobart, Tasmania, for analysing the grab water samples.

While preparing this manuscript, the authors used Generative AI to improve language clarity and readability. All AI-generated suggestions were carefully reviewed and edited as necessary, and the authors take full

responsibility for the final content of the publication.

Data availability

The code and data are available at: <https://github.com/yiqing-csiro/wq-meta-learning-public>.

References

- Abd-Elrahman, A., Croxton, M., Pande-Chettri, R., Toor, G.S., Smith, S., Hill, J., 2011. In situ estimation of water quality parameters in freshwater aquaculture ponds using hyperspectral imaging system. *ISPRS Journal of Photogrammetry and Remote Sensing* 66, 463–472. doi:<https://doi.org/10.1016/j.isprsjprs.2011.02.005>.
- Anderson, D.M., Cembella, A.D., Hallegraeff, G.M., 2012. Progress in understanding harmful algal blooms: paradigm shifts and new technologies for research, monitoring, and management. *Annual Review of Marine Science* 4, 143–176. doi:<https://doi.org/10.1146/annurev-marine-120308-081121>.
- Babin, M., Stramski, D., Ferrari, G.M., Claustre, H., Bricaud, A., Obolensky, G., Hoepffner, N., 2003. Variations in the light absorption coefficients of phytoplankton, nonalgal particles, and dissolved organic matter in coastal waters around Europe. *Journal of Geophysical Research: Oceans* 108, 3211. doi:<https://doi.org/10.1029/2001JC000882>.
- Baker, E.T., Lavelle, J.W., 1984. The effect of particle size on the light attenuation coefficient of natural suspensions. *Journal of Geophysical Research: Oceans* 89, 8197–8203. doi:<https://doi.org/10.1029/JC089iC05p08197>.
- Blondeau-Patissier, D., Brando, V.E., Oubelkheir, K., Dekker, A.G., Clementson, L.A., Daniel, P., 2009. Bio-optical variability of the absorption and scattering properties of the Queensland inshore and reef waters, Australia. *Journal of Geophysical Research: Oceans* 114, C05003. doi:<https://doi.org/10.1029/2008JC005039>.
- Boss, E., Pegau, W.S., 2001. Relationship of light scattering at an angle in the backward direction to the backscattering coefficient. *Applied Optics* 40, 5503–5507. doi:<https://doi.org/10.1364/AO.40.005503>.
- Chabrillat, S., Foerster, S., Segl, K., Beamish, A., Brell, M., Asadzadeh, S., Milewski, R., Ward, K.J., Brosinsky, A., Koch, K., et al., 2024. The EnMAP spaceborne imaging spectroscopy mission: Initial scientific results two years after launch. *Remote Sensing of Environment* 315, 114379. doi:<https://doi.org/10.1016/j.rse.2024.114379>.

- Cherukuru, N., Brando, V.E., Blondeau-Patissier, D., Ford, P.W., Clementson, L.A., Robson, B.J., 2017. Impact of wet season river flood discharge on phytoplankton absorption properties in the southern Great Barrier Reef region coastal waters. *Estuarine, Coastal and Shelf Science* 196, 379–386. doi:<https://doi.org/10.1016/j.ecss.2017.07.023>.
- Cherukuru, N., Brando, V.E., Schroeder, T., Clementson, L.A., Dekker, A.G., 2014. Influence of river discharge and ocean currents on coastal optical properties. *Continental Shelf Research* 84, 188–203. doi:<https://doi.org/10.1016/j.csr.2014.04.022>.
- Cherukuru, N., Davies, P.L., Brando, V.E., Anstee, J.M., Baird, M.E., Clementson, L.A., Doblin, M.A., 2016a. Physical oceanographic processes influence bio-optical properties in the Tasman Sea. *Journal of Sea Research* 110, 1–7. doi:<https://doi.org/10.1016/j.seares.2016.01.008>.
- Cherukuru, N., Dekker, A.G., Hardman-Mountford, N.J., Clementson, L.A., Thompson, P.A., 2019. Bio-optical variability in multiple water masses across a tropical shelf: Implications for ocean colour remote sensing models. *Estuarine, Coastal and Shelf Science* 219, 223–230. doi:<https://doi.org/10.1016/j.ecss.2019.02.015>.
- Cherukuru, N., Ford, P.W., Matear, R.J., Oubelkheir, K., Clementson, L.A., Suber, K., Steven, A.D., 2016b. Estimating dissolved organic carbon concentration in turbid coastal waters using optical remote sensing observations. *International Journal of Applied Earth Observation and Geoinformation* 52, 149–154. doi:<https://doi.org/10.1016/j.jag.2016.06.010>.
- Cherukuru, N., Martin, P., Sanwlani, N., Mujahid, A., Müller, M., 2020. A semi-analytical optical remote sensing model to estimate suspended sediment and dissolved organic carbon in tropical coastal waters influenced by peatland-draining river discharges off Sarawak, Borneo. *Remote Sensing* 13, 99. doi:<https://doi.org/10.3390/rs13010099>.
- Choo, J., Cherukuru, N., Lehmann, E., Paget, M., Mujahid, A., Martin, P., Müller, M., 2022. Spatial and temporal dynamics of suspended sediment concentrations in coastal waters of the South China Sea, off Sarawak, Borneo: ocean colour remote sensing observations and analysis. *Biogeosciences* 19, 5837–5857. doi:<https://doi.org/10.5194/bg-19-5837-2022>.
- De Valck, J., Rolfe, J., 2018. Linking water quality impacts and benefits of ecosystem services in the Great Barrier Reef. *Marine Pollution Bulletin* 130, 55–66. doi:<https://doi.org/10.1016/j.marpolbul.2018.03.017>.
- Deisenroth, M.P., Faisal, A.A., Ong, C.S., 2020. *Mathematics for Machine Learning*. Cambridge University Press. doi:<https://doi.org/10.1017/9781108679930>.

- Del Vecchio, R., Blough, N.V., 2004. Spatial and seasonal distribution of chromophoric dissolved organic matter and dissolved organic carbon in the Middle Atlantic Bight. *Marine Chemistry* 89, 169–187. doi:<https://doi.org/10.1016/j.marchem.2004.02.027>.
- Finn, C., Abbeel, P., Levine, S., 2017. Model-agnostic meta-learning for fast adaptation of deep networks, in: *International Conference on Machine Learning*, PMLR. pp. 1126–1135. URL: <https://proceedings.mlr.press/v70/finn17a.html>.
- Gui, S., Murphy, K.A., Tischer, M.A., Weavers, L.K., Qin, R., 2026. Enhanced remote sensing of surface water Chlorophyll-a: Coupling dynamic algae vertical movement modeling with multi-spectral satellite images. *ISPRS Journal of Photogrammetry and Remote Sensing* 234, 205–226. doi:<https://doi.org/10.1016/j.isprsjprs.2026.02.028>.
- Guo, Y., Cherukuru, N., Lehmann, E., Qi, X., Doubell, M.J., Kesav Unnithan, S., Feng, M., 2025a. Decadal analysis of sea surface temperature patterns, climatology, and anomalies in temperate coastal waters with Landsat-8 TIRS observations. *GIScience & Remote Sensing* 62, 2518623. doi:<https://doi.org/10.1080/15481603.2025.2518623>.
- Guo, Y., Cherukuru, N., Lehmann, E., Unnithan, S.K., Kerrisk, G., Malthus, T., Islam, F., 2025b. Hyperspectral in situ remote sensing of water surface nitrate in the Fitzroy River estuary, Queensland, Australia, using deep learning, in: *2025 IEEE International Geoscience and Remote Sensing Symposium*, IEEE. pp. 4798–4802. doi:<https://doi.org/10.1109/IGARSS55030.2025.11313913>.
- Guo, Y., Jia, X., Paull, D., Benediktsson, J.A., 2019. Nomination-favoured opinion pool for optical-SAR-synergistic rice mapping in face of weakened flooding signals. *ISPRS Journal of Photogrammetry and Remote Sensing* 155, 187–205. doi:<https://doi.org/10.1016/j.isprsjprs.2019.07.008>.
- Guo, Y., Mokany, K., Ong, C., Moghadam, P., Ferrier, S., Levick, S., 2022. Quantitative assessment of DESIS hyperspectral data for plant biodiversity estimation in Australia, in: *2022 IEEE International Geoscience and Remote Sensing Symposium*, IEEE. pp. 1744–1747. doi:<https://doi.org/10.1109/IGARSS46834.2022.9883033>.
- Guo, Y., Mokany, K., Ong, C., Moghadam, P., Ferrier, S., Levick, S.R., 2023. Plant species richness prediction from DESIS hyperspectral data: A comparison study on feature extraction procedures and regression models. *ISPRS Journal of Photogrammetry and Remote Sensing* 196, 120–133. doi:<https://doi.org/10.1016/j.isprsjprs.2022.12.028>.

- Hansell, D.A., Carlson, C.A., 1998. Deep-ocean gradients in the concentration of dissolved organic carbon. *Nature* 395, 263–266. doi:<https://doi.org/10.1038/26200>.
- Hansell, D.A., Carlson, C.A., Repeta, D.J., Schlitzer, R., 2009. Dissolved organic matter in the ocean: A controversy stimulates new insights. *Oceanography* 22, 202–211. doi:<https://doi.org/10.5670/oceanog.2009.109>.
- Huot, Y., Babin, M., Bruyant, F., Grob, C., Twardowski, M., Claustre, H., 2007. Relationship between photosynthetic parameters and different proxies of phytoplankton biomass in the subtropical ocean. *Biogeosciences* 4, 853–868. doi:<https://doi.org/10.5194/bgd-4-707-2007>.
- Jiang, D., Matsushita, B., Pahlevan, N., Gurlin, D., Fichot, C.G., Harringmeyer, J., Sent, G., Brito, A.C., Brotas, V., Werther, M., et al., 2023. Estimating the concentration of total suspended solids in inland and coastal waters from Sentinel-2 MSI: A semi-analytical approach. *ISPRS Journal of Photogrammetry and Remote Sensing* 204, 362–377. doi:<https://doi.org/10.1016/j.isprsjprs.2023.09.020>.
- Krutz, D., Müller, R., Knodt, U., Günther, B., Walter, I., Sebastian, I., Säuberlich, T., Reulke, R., Carmona, E., Eckardt, A., et al., 2019. The instrument design of the DLR earth sensing imaging spectrometer (DESI). *Sensors* 19, 1622. doi:<https://doi.org/10.3390/s19071622>.
- Lee, Z., Carder, K.L., Arnone, R.A., 2002. Deriving inherent optical properties from water color: a multiband quasi-analytical algorithm for optically deep waters. *Applied Optics* 41, 5755–5772. doi:<https://doi.org/10.1364/AO.41.005755>.
- Lehmann, M.K., Gurlin, D., Pahlevan, N., Alikas, K., Conroy, T., Anstee, J., Balasubramanian, S.V., Barbosa, C.C., Binding, C., Bracher, A., et al., 2023. GLORIA - A globally representative hyperspectral in situ dataset for optical sensing of water quality. *Scientific Data* 10, 100. doi:<https://doi.org/10.1038/s41597-023-01973-y>.
- Lou, J., Liu, B., Xiong, Y., Zhang, X., Yuan, X., 2025. Variational autoencoder framework for hyperspectral retrievals (Hyper-VAE) of phytoplankton absorption and chlorophyll a in coastal waters for NASA’s EMIT and PACE missions. *IEEE Transactions on Geoscience and Remote Sensing* 63, 1–16. doi:<https://doi.org/10.1109/TGRS.2025.3566417>.
- Luo, C., Xiang, W., Han, K., Yu, L., Guo, Y., Unnithan, S.K., Qi, X., Cherukuru, N., 2025. HyperEst: Context-aware self-supervised pretraining for hyperspectral and multispectral water quality estimation. *International Journal of Applied Earth Observation and Geoinformation* 143, 104761. doi:<https://doi.org/10.1016/j.jag.2025.104761>.

- Manzo, C., Bresciani, M., Giardino, C., Braga, F., Bassani, C., 2015. Sensitivity analysis of a bio-optical model for Italian lakes focused on Landsat-8, Sentinel-2 and Sentinel-3. *European Journal of Remote Sensing* 48, 17–32. doi:<https://doi.org/10.5721/EuJRS20154802>.
- Mao, Z., Chen, J., Pan, D., Tao, B., Zhu, Q., 2012. A regional remote sensing algorithm for total suspended matter in the East China Sea. *Remote Sensing of Environment* 124, 819–831. doi:<https://doi.org/10.1016/j.rse.2012.06.014>.
- Medina, L.B., Nguyen, D., Joehnk, K., Guo, Y., Deo, R.C., Prasad, S., 2026. Data-driven prediction of dissolved oxygen to identify fish kill factors: Case study in Redbank weir at Murrumbidgee River, Australia. *Ecological Informatics* 95, 103778. doi:<https://doi.org/10.1016/j.ecoinf.2026.103778>.
- Mélin, F., Vantrepotte, V., 2015. How optically diverse is the coastal ocean? *Remote Sensing of Environment* 160, 235–251. doi:<https://doi.org/10.1016/j.rse.2015.01.023>.
- Mobley, C.D., 1989. A numerical model for the computation of radiance distributions in natural waters with wind-roughened surfaces. *Limnology and Oceanography* 34, 1473–1483. doi:<https://doi.org/10.4319/lo.1989.34.8.1473>.
- Mobley, C.D., 1999. Estimation of the remote-sensing reflectance from above-surface measurements. *Applied Optics* 38, 7442–7455. doi:<https://doi.org/10.1364/AO.38.007442>.
- Neil, C., Spyrakos, E., Hunter, P.D., Tyler, A.N., 2019. A global approach for chlorophyll-a retrieval across optically complex inland waters based on optical water types. *Remote Sensing of Environment* 229, 159–178. doi:<https://doi.org/10.1016/j.rse.2019.04.027>.
- Nelson, N.B., Siegel, D.A., 2013. The global distribution and dynamics of chromophoric dissolved organic matter. *Annual Review of Marine Science* 5, 447–476. doi:<https://doi.org/10.1146/annurev-marine-120710-100751>.
- Novoa, S., Wernand, M., Van der Woerd, H., 2013. The Forel-Ule scale revisited spectrally: preparation protocol, transmission measurements and chromaticity. *Journal of the European Optical Society-Rapid Publications* 8, 13057. doi:<https://doi.org/10.2971/jeos.2013.13057>.
- Ogashawara, I., Mishra, D.R., Nascimento, R.F., Alcantara, E.H., Kampel, M., Stech, J.L., 2016. Re-parameterization of a quasi-analytical algorithm for colored dissolved organic matter dominant inland waters. *International Journal of Applied Earth Observation and Geoinformation* 53, 128–145. doi:<https://doi.org/10.1016/j.jag.2016.09.001>.

- O'Shea, R.E., Pahlevan, N., Smith, B., Boss, E., Gurlin, D., Alikas, K., Kangro, K., Kudela, R.M., Vaičiūtė, D., 2023. A hyperspectral inversion framework for estimating absorbing inherent optical properties and biogeochemical parameters in inland and coastal waters. *Remote Sensing of Environment* 295, 113706. doi:<https://doi.org/10.1016/j.rse.2023.113706>.
- Oubelkheir, K., Clementson, L.A., Webster, I.T., Ford, P.W., Dekker, A.G., Radke, L.C., Daniel, P., 2006. Using inherent optical properties to investigate biogeochemical dynamics in a tropical macrotidal coastal system. *Journal of Geophysical Research: Oceans* 111. doi:<https://doi.org/10.1029/2005JC003113>.
- Oubelkheir, K., Ford, P.W., Cherukuru, N., Clementson, L.A., Petus, C., Devlin, M., Schroeder, T., Steven, A.D., 2023. Impact of a tropical cyclone on terrestrial inputs and bio-optical properties in Princess Charlotte Bay (Great Barrier Reef lagoon). *Remote Sensing* 15, 652. doi:<https://doi.org/10.3390/rs15030652>.
- Oubelkheir, K., Ford, P.W., Clementson, L.A., Cherukuru, N., Fry, G., Steven, A.D., 2014. Impact of an extreme flood event on optical and biogeochemical properties in a subtropical coastal periurban embayment (Eastern Australia). *Journal of Geophysical Research: Oceans* 119, 6024–6045. doi:<https://doi.org/10.1002/2014JC010205>.
- Pan, X., Wong, G.T., Ho, T.Y., Tai, J.H., Liu, H., Liu, J., Shiah, F.K., 2018. Remote sensing of surface [nitrite+nitrate] in river-influenced shelf-seas: The northern South China Sea Shelf-sea. *Remote Sensing of Environment* 210, 1–11. doi:<https://doi.org/10.1016/j.rse.2018.03.012>.
- Pignatti, S., Palombo, A., Pascucci, S., Romano, F., Santini, F., Simoniello, T., Umberto, A., Vincenzo, C., Acito, N., Diani, M., et al., 2013. The PRISMA hyperspectral mission: Science activities and opportunities for agriculture and land monitoring, in: 2013 IEEE International Geoscience and Remote Sensing Symposium, IEEE. pp. 4558–4561. doi:<https://doi.org/10.1109/IGARSS.2013.6723850>.
- Pope, R.M., Fry, E.S., 1997. Absorption spectrum (380–700 nm) of pure water. II. integrating cavity measurements. *Applied Optics* 36, 8710–8723. doi:<https://doi.org/10.1364/AO.36.008710>.
- Röttgers, R., McKee, D., Utschig, C., 2014. Temperature and salinity correction coefficients for light absorption by water in the visible to infrared spectral region. *Optics Express* 22, 25093–25108. doi:<https://doi.org/10.1364/OE.22.025093>.
- Saltelli, A., Tarantola, S., Chan, K.S., 1999. A quantitative model-independent method for global sensitivity analysis of model output. *Technometrics* 41, 39–56. doi:<https://doi.org/10.1080/00401706.1999.10485594>.

- Schaffelke, B., Carleton, J., Skuza, M., Zagorskis, I., Furnas, M.J., 2012. Water quality in the inshore Great Barrier Reef lagoon: Implications for long-term monitoring and management. *Marine Pollution Bulletin* 65, 249–260. doi:<https://doi.org/10.1016/j.marpolbul.2011.10.031>.
- Seegers, B.N., Stumpf, R.P., Schaeffer, B.A., Loftin, K.A., Werdell, P.J., 2018. Performance metrics for the assessment of satellite data products: an ocean color case study. *Optics Express* 26, 7404–7422. doi:<https://doi.org/10.1364/OE.26.007404>.
- Spyrakos, E., O'donnell, R., Hunter, P.D., Miller, C., Scott, M., Simis, S.G., Neil, C., Barbosa, C.C., Binding, C.E., Bradt, S., et al., 2018. Optical types of inland and coastal waters. *Limnology and Oceanography* 63, 846–870. doi:<https://doi.org/10.1002/lno.10674>.
- Unnithan, S.K., Cherukuru, N., Ingleton, T., Lehmann, E., Paget, M., Guo, Y., Drayson, N., Kerrisk, G., 2025. Mapping total suspended solids (TSS) and dissolved organic carbon (DOC) in complex coastal waters using deep learning enhanced remote sensing. *Ecological Informatics* 90, 103276. doi:<https://doi.org/10.1016/j.ecoinf.2025.103276>.
- Werdell, P.J., Franz, B.A., Bailey, S.W., Feldman, G.C., Boss, E., Brando, V.E., Dowell, M., Hirata, T., Lavender, S.J., Lee, Z., Loisel, H., Maritorena, S., Mélin, F., Moore, T.S., Smyth, T.J., Antoine, D., Devred, E., Doxaran, D., Fanton d'Andon, O.H., Mangin, A., 2013. Generalized ocean color inversion model for retrieving marine inherent optical properties. *Applied Optics* 52, 2019–2037. doi:<https://doi.org/10.1364/AO.52.002019>.
- Wernand, M., Van der Woerd, H., 2010. Spectral analysis of the Forel-Ule ocean colour comparator scale. *Journal of the European Optical Society-Rapid Publications* 5, 10014s. doi:<https://doi.org/10.2971/jeos.2010.10014s>.
- Yang, J., Zhang, H., Guo, Y., Donohue, R.J., McVicar, T.R., Ferrier, S., Müller, W., Lü, X., Fang, Y., Wang, X., et al., 2025. Globally mapping the nitrogen stable isotope ratios of terrestrial vegetation from 1984 to 2022. *Earth's Future* 13, e2024EF005836. doi:<https://doi.org/10.1029/2024EF005836>.
- Zhang, L., Ma, C., Chen, X., Zhang, C., Li, Q., Ye, X., Tian, L., 2025. An integrated algorithm to estimate chlorophyll-a concentration in various optical waters using HY-3A CZI. *ISPRS Journal of Photogrammetry and Remote Sensing* 225, 402–422. doi:<https://doi.org/10.1016/j.isprsjprs.2025.05.001>.
- Zhao, F., Guo, Y., Huang, Y., Reddy, K.N., Lee, M.A., Fletcher, R.S., Thomson, S.J., 2014a. Early detection of crop injury from herbicide glyphosate by leaf biochemical parameter inversion. *International Journal of Applied Earth Observation and Geoinformation* 31, 78–85. doi:<https://doi.org/10.1016/j.jag.2014.03.010>.

- Zhao, F., Huang, Y., Guo, Y., Reddy, K.N., Lee, M.A., Fletcher, R.S., Thomson, S.J., 2014b. Early detection of crop injury from glyphosate on soybean and cotton using plant leaf hyperspectral data. *Remote Sensing* 6, 1538–1563. doi:<https://doi.org/10.3390/rs6021538>.
- Zhao, F., Ma, W., Zhao, J., Guo, Y., Tariq, M., Li, J., 2024. Global retrieval of the spectrum of terrestrial chlorophyll fluorescence: First results with TROPOMI. *Remote Sensing of Environment* 300, 113903. doi:<https://doi.org/10.1016/j.rse.2023.113903>.
- Zhi, W., Appling, A.P., Golden, H.E., Podgorski, J., Li, L., 2024. Deep learning for water quality. *Nature Water* 2, 228–241. doi:<https://doi.org/10.1038/s44221-024-00202-z>.